# The Vertical Distribution of Radon in Clear and Cloudy Daytime Terrestrial Boundary Layers

ALASTAIR G. WILLIAMS, WLODEK ZAHOROWSKI, SCOTT CHAMBERS, AND ALAN GRIFFITHS
*Australian Nuclear Science and Technology Organisation, Sydney, New South Wales, Australia*

JÖRG M. HACKER
*Airborne Research Australia, Flinders University of South Australia, Adelaide, South Australia, Australia*

ADRIAN ELEMENT AND SYLVESTER WERCZYNSKI
*Australian Nuclear Science and Technology Organisation, Sydney, New South Wales, Australia*

(Manuscript received 8 June 2010, in final form 6 August 2010)

## ABSTRACT

Radon ($^{222}$Rn) is a powerful natural tracer of mixing and exchange processes in the atmospheric boundary layer. The authors present and discuss the main features of a unique dataset of 50 high-resolution vertical radon profiles up to 3500 m above ground level, obtained in clear and cloudy daytime terrestrial boundary layers over an inland rural site in Australia using an instrumented motorized research glider. It is demonstrated that boundary layer radon profiles frequently exhibit a complex layered structure as a result of mixing and exchange processes of varying strengths and extents working in clear and cloudy conditions within the context of the diurnal cycle and the synoptic meteorology. Normalized aircraft radon measurements are presented, revealing the characteristic structure and variability of three major classes of daytime boundary layer: 1) dry convective boundary layers, 2) mixed layers topped with residual layers, and 3) convective boundary layers topped with coupled nonprecipitating clouds. Robust and unambiguous signatures of important atmospheric processes in the boundary layer are identifiable in the radon profiles, including ''top-down'' mixing associated with entrainment in clear-sky cases and strongly enhanced venting and subcloud-layer mixing when substantial active cumulus are present. In poorly mixed conditions, radon gradients in the daytime atmospheric surface layer significantly exceed those predicted by Monin–Obukhov similarity theory. In two case studies, it is demonstrated for the first time that a sequence of vertical radon profiles measured over the course of a single day can consistently reproduce major structural features of the evolving boundary layer.

## 1. Introduction

Radon-222 (radon) is a naturally occurring radioactive noble gas of terrestrial origin, commonly used for atmospheric tracer studies (e.g., Zahorowski et al. 2004). Applications of radon have included

1) Selection of least-perturbed marine air masses for baseline studies (Zahorowski and Whittlestone 1999);
2) Tracing of terrestrial air mass movements (Israël 1951; Polian et al. 1986; Kritz et al. 1990; Balkanski et al. 1992; Perry et al. 1999), including the refinement of source footprints for aerosols in continental outflow events (Zahorowski et al. 2005; Crawford et al. 2008);
3) Calibration of regionally integrated emissions of important greenhouse gases (Kirichenko 1970; Gaudry et al. 1990; Schmidt et al. 1996; Biraud et al. 2000; Williams et al. 2009);
4) Evaluation of the performance of transport and mixing schemes in weather, climate, and chemical transport models (Jacob et al. 1997; Dentener et al. 1999; Rasch et al. 2000; Chevillard et al. 2002; Gupta et al. 2004; Considine et al. 2005; Forster et al. 2007);
5) Electric field studies (Jonassen and Wilkening 1970; Anderson and Larson 1974); and
6) Quantification of vertical mixing in the lower atmosphere (Wigand and Wenk 1928; Jacobi and André

---

*Corresponding author address:* Alastair Williams, Australian Nuclear Science and Technology Organisation, Locked Bag 2001, Kirrawee DC, NSW 2232, Australia.
E-mail: alastair.williams@ansto.gov.au

DOI: 10.1175/2010JAS3576.1

TABLE 1. Reported airborne radon profile observations by altitude and surface type. Asterisks indicate studies reproduced in Fig. 6b.

| ABL ($z < 5$ km AGL) | | ABL-troposphere ($z < 13$ km AGL) | | |
|---|---|---|---|---|
| Inland | Coast/island/ocean | Inland | Coast/island/ocean | Troposphere–stratosphere |
| Wigand and Wenk (1928)* | Miranda (1957) | Kirichenko (1962)* | Wexler et al. (1956) | Machta and Lucas (1962) |
| Wilkening (1956) | Nguyen et al. (1967) | Kirichenko (1970)* | Ramonet et al. (1996) | Machta (1963) |
| Wilkening and Paltridge (1967) | Polian et al. (1986) | Nazarov et al. (1970)* | Kritz et al. (1998) | Kritz et al. (1990) |
| Birot et al. (1968) | Andreae et al. (1988) | Moore et al. (1973)* | Moore et al. (1977) | Lambert et al. (1990) |
| Bradley and Pearson (1970)* | Zaucker et al. (1996) | | | Kritz et al. (1993) |
| Wilkening (1970)* | Lee and Larson (1997) | | | |
| Jonassen and Wilkening (1970)* | | | | |
| Larson and Hoppel (1973)* | | | | |
| Anderson and Larson (1974)* | | | | |
| Larson (1974) | | | | |
| Pereira et al. (1988) | | | | |
| Guedalia et al. (1974)* | | | | |

1963; Guedalia et al. 1974; Liu et al. 1984; Butterweck et al. 1994; Zaucker et al. 1996; Lee and Larson 1997).

The popularity of radon as an atmospheric tracer is largely a result of its useful properties. Produced via the $\alpha$ decay of long-lived radium-226, present in most rock and soil types, it is the only gaseous decay product of the uranium-238 series. This results in a fairly consistent flux density of radon from ice-free terrestrial surfaces of between 0.72 and 1.2 atoms per centimeter squared per second (15–25 mBq $m^{-2}$ $s^{-1}$), which varies mainly with soil moisture and its composition, porosity, and permeability (e.g., Griffiths et al. 2010). For tracing of air transport in the atmospheric boundary layer (ABL) over land, the radon source function can be assumed to be approximately constant over the diurnal cycle, and horizontally uniform on local scales (Jacob et al. 1997). Over open water bodies, radon emissions are two to three orders of magnitude smaller than over land (Turekian et al. 1977; Lambert et al. 1982; Schery and Huang 2004).

Being inert and poorly soluble in water (Jacob and Prather 1990; Li and Chang 1996), radon is not susceptible to wet or dry atmospheric removal processes. In fact, radon's only significant atmospheric sink is radioactive decay, and its half-life of 3.82 days is comparable to the residence time of key atmospheric pollutants and the synoptic time scale. This half-life is well suited for ABL studies, as it is long compared with typical turbulent time scales (<1 h) but short enough to constrain radon concentrations in the free troposphere to be typically two orders of magnitude lower than average ABL values. The result is large concentration variations through the lower troposphere that are principally related to vertical mixing processes.

Although the benefits of understanding the processes affecting radon in the atmosphere have long been recognized, detailed knowledge of the vertical distribution of radon in the ABL is lacking. Most reported tower-based studies probe only the first 5–40 m of the atmosphere (e.g., Moses et al. 1960; Gogolak and Beck 1980; Butterweck et al. 1994), and although there are a few tall towers that extend deep enough to cover the entire nocturnal stable boundary layer (100–300 m; e.g., Hosler 1968; Cohen et al. 1972; Zahorowski et al. 2008), these can at best achieve only partial coverage of the daytime convective mixed layer. Aircraft measurements can probe the entire troposphere, but airborne radon datasets exhibiting high vertical resolution in the ABL are rare [see reviews in Lambert et al. (1982), Liu et al. (1984), and Koch et al. (2006)].

Table 1 lists major published studies utilizing airborne radon (or radon progeny) measurements. The studies differ in their motivation, range of altitudes (near-surface to stratosphere), and geographical locations (inland, coastal, islands, and open ocean). Given the huge radon flux density gradient across the coast and resulting complications, inland sites are most practical for investigations of ABL vertical processes. Of the 31 investigations listed in Table 1, only 12 focus on the structure of the inland ABL (left-most column). The number of complete radon profiles reported in these 12 studies varied from 3 to 30, with none resolving the ABL to more than four altitudes. In addition, most observations were collected in cloud-free conditions (preferred for radon progeny measurements). This fair-weather bias in existing radon profile observations has led to considerable uncertainty in the impact of clouds on the ABL radon distribution (Liu et al. 1984; Lin et al. 1996).

Of the inland ABL studies, Guedalia et al. (1974) and Wilkening (1970) report the greatest data coverage. Guedalia et al. (1974) report on 30 profiles between 100 and 3000 m, collected over a year at a site 200 km from the coast in France, using radon progeny measurements. The main focus of their study was the determination of vertical eddy diffusion coefficients targeting clear-sky conditions. Wilkening (1970) collected 12 radon profiles over a 3-yr period, including morning and afternoon flights in clear skies as well as nonprecipitating cumulus conditions. Jonassen and Wilkening (1970) also report seasonally resolved profiles (five winter flights, four summer flights). However, both these studies were conducted over complex terrain in the Rio Grande Valley.

In this paper, we present and analyze the main features of a unique dataset of high-resolution vertical radon profiles up to 3500 m above ground level (AGL) over simple terrain. These profiles resolve the ABL to either 6 or 10 altitudes. A series of four experimental field campaigns in rural inland Australia is described, featuring aircraft-based measurements of radon in and above the daytime boundary layer in both clear and cloudy conditions. The 50 high-resolution radon profiles collected during the campaigns are classified and tabulated according to prevailing weather conditions. Surface radon time series and surface layer gradients are discussed, and then vertical radon profiles are presented for three major classes of boundary layer. Results are discussed in relation to pertinent atmospheric mixing and exchange processes. Finally, two case studies are presented illustrating the variability of vertical radon distributions in the ABL.

## 2. Methods and measurements

### a. *Airborne radon sampling system*

Aircraft measurements have previously been used to determine vertical radon profiles from several hundred meters to more than 10 km AGL (Table 1). Approaches used have relied either on radon or radon progeny measurements, sometimes referred to as direct and indirect techniques, respectively.

Radon measurements involve either flask sampling (Kritz et al. 1990, 1998) or absorption of radon present in the sampled air in situ onto cold plates (Wigand and Wenk 1928) or activated charcoal (Miranda 1957; Machta and Lucas 1962; Moore et al. 1977; Zaucker et al. 1996) with subsequent laboratory extraction. This method yields unambiguous radon concentrations, with two main disadvantages: 1) the method requires an extraction and counting facility to be in close proximity to minimize decay and charcoal in-growth time between sampling and radon extraction; and 2) radon extraction is a labor intensive process, which can only partially be simplified by automation and computer-controlled laboratory processes. Radon progeny measurements, on the other hand, are made by filtering (Filippi 2000) or electrostatically precipitating (Negro et al. 1996) radon progeny for in situ alpha-particle counting. This method does not have the disadvantages of the radon measurements mentioned above, and consequently it has fewer restrictions on the number of samples that can be collected per flight (Lambert et al. 1990). However, it crucially relies on assumptions regarding the equilibrium between radon and its progeny, which is highly variable in space and time.

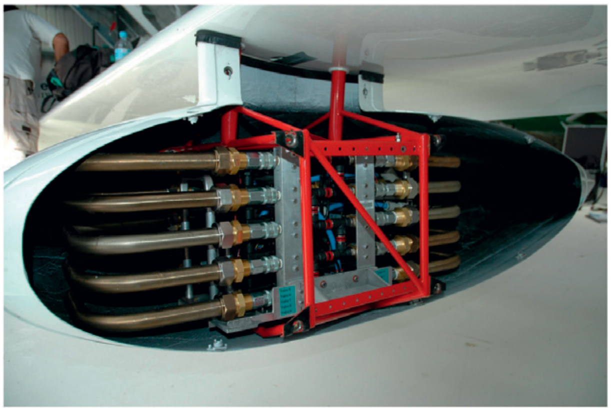

FIG. 1. 10-trap radon sampler, installed in an underwing pod of the ECO-Dimona instrumented motorized glider operated by Airborne Research Australia.

In this paper, we report on radon measurements in the atmospheric boundary layer, gathered from an airborne platform using a charcoal trap sampling system similar to that of Zaucker et al. (1996). The sampler (Fig. 1) can capture up to 10 radon samples per flight and is small and light enough (23 kg) to be mounted in the underwing pod of a motorized research glider. The simple architecture features a compact arrangement of U-shaped stainless steel sampling tubes (25 mm in diameter, 60 cm long), connected via quick-release fittings to a manifold of electronically controlled solenoid valves and a 24-V dual membrane pump. The system power consumption at 220 W is minimal, and solid-state logging electronics enable flights up to high altitudes. The version of the sampler shown in Fig. 1 was used in the most recent campaign reported here; the other three campaigns used a version that allowed only six samples per flight. Each sampling tube has a volume of 290 $\mathrm{cm}^3$, holding approximately 110 g of 0.9−1.7-mm activated coconut shell charcoal. Samples are collected over 5- or 10-min intervals, depending on the expected magnitude of radon concentration, at a flow rate of 20–30 L $\mathrm{min}^{-1}$ at standard temperature and pressure. Any ambient radon is removed from the traps immediately prior to the flight by heating them to 350°C and purging with conditioned nitrogen for 20 min. After landing, the charcoal traps are removed and transported to the counting laboratory, resulting in a delay of approximately 4 h between radon collection and extraction. The laboratory extraction procedure is described in appendix A.

The lower limit of detection, defined as the radon concentration in the sampled air for which the counting error reaches 30%, is better than 10 mBq $m^{-3}$ (<5 atoms per liter). The total uncertainty in the atmospheric radon concentration estimates, however, also depends on other uncertainties within the system, including variability of the counting efficiency [~5% relative standard deviation (RSD)], accuracy of the radon calibrated source (±4%) and, above all, the uncertainty of determination of the radon in-growth in the sampling trap due to the presence of radium-226 (radon's parent element) in the charcoal. Since the trace levels of radium-226 activity can vary substantially with charcoal batch and packing density, the background in-growth rate has been characterized for every sampling tube individually. For each radon sample collected, a background count is estimated, based on the particular sample tube used and the time elapsed between initial flushing (prior to exposure) and laboratory extraction. The variability of the in-growth rates results in estimated uncertainties that are different for each sample. The distribution of the estimated uncertainties can be characterized statistically using a lognormal form with a geometric mean of 104 mBq $m^{-3}$ (1-$\sigma$ range: 40–275 mBq $m^{-3}$). Comparison of this with the geometric mean of 1354 mBq $m^{-3}$ (1-$\sigma$ range: 280–6547 mBq $m^{-3}$) for the calculated atmospheric radon concentrations indicates that typical errors for this technique are around 8%.

### b. *Field measurements*

Over a period of 2 yr, four 2-week airborne field campaigns were conducted (May 2006, January 2007, May 2007, and May 2008), collecting radon and supporting meteorological data from aircraft and ground-based instrumentation in clear and cloudy daytime boundary layers over rural inland Australia. Based out of Goulburn Airport (34°48.4′S, 149°44.2′E), twice-daily flights were conducted over the center of a broad shallow valley in the Southern Tablelands region of New South Wales (600–700 m above sea level). The terrain under the flight pattern was fairly flat, dry, and uniform and is used mainly as grazing pasture in this low-rainfall region. Being more than 100 km inland, the site is free of the influences of coastal circulations.

Flights were conducted with an instrumented ECO-Dimona motorized glider operated by Airborne Research Australia. The Dimona simultaneously recorded numerous meteorological and navigational quantities. Flights typically lasted 2–3 h and reached maximum altitudes of around 3.5 km AGL. Patterns commenced with a sounding (rapid ascent) to achieve position over the chosen site and identify important layers and levels, including the mixed layer depth and cloud base/top when boundary layer clouds were present. This was followed by a simple descending vertical stack of straight-and-level sampling runs, usually of 5-min duration (~10 km at typical flight speeds) and spaced to include

1) the ''clean'' air well above the top of the boundary layer,
2) the cloud layer (if present),
3) levels just above and below the top of the main mixed layer (or cloud base),
4) the midpart of the mixed layer (subcloud layer), and
5) always one run close to the surface (usually about 30 m AGL).

As the aircraft operated under visual flight rules (VFR) for these flights, it was not permitted to fly inside clouds. Therefore, no flights were conducted in overcast conditions, and the data collected in the cloud layer are mainly representative of intercloud air.

A 10-m mast erected at a nearby farm recorded continuous meteorological information during the campaigns, and near-surface (2 m) radon concentrations were monitored on an hourly basis using a 1500-L dual-flow loop, two-filter detector (Zahorowski et al. 2005).

Independent of the aircraft campaigns, two ground-based surveys were conducted in August 2006 and February 2008 using an emanometer based on the flow-through accumulator method (Zahorowski and Whittlestone 1996) to make point measurements of surface radon flux densities in the Goulburn area (Griffiths et al. 2010). These measurements were made on a geographical grid that included the flight region. Mean fluxes obtained were 18 ± 9 mBq $m^{-2}$ $s^{-1}$ for August 2006 and 28 ± 13 mBq $m^{-2}$ $s^{-1}$ for February 2008.

### c. *Classification of flights*

The aircraft radon dataset used in this study is documented in appendix B. Table B1 presents the naming conventions and categorizations for the Goulburn flights, together with information on layer depths, clouds, and weather conditions. Here and elsewhere in the text, $h_{ML}$, $h_{RL}$, $h_{CB}$, and $h_{CT}$ are the altitudes (m AGL) of the top of the mixed and residual layers, cloud base, and cloud top, respectively, derived from aircraft ascents and observations. Boundary layer stability categories are based on the bulk stability parameter $-h_{ML}/L$, where $L$ is the Obukhov length.

Of the 50 flights, 19 were flown in dry convective boundary layers with little or no cloud, 10 were flown in boundary layers topped with residual layers, and 21 were flown in boundary layers topped with substantial coupled cloud layers. No flights were conducted in precipitating

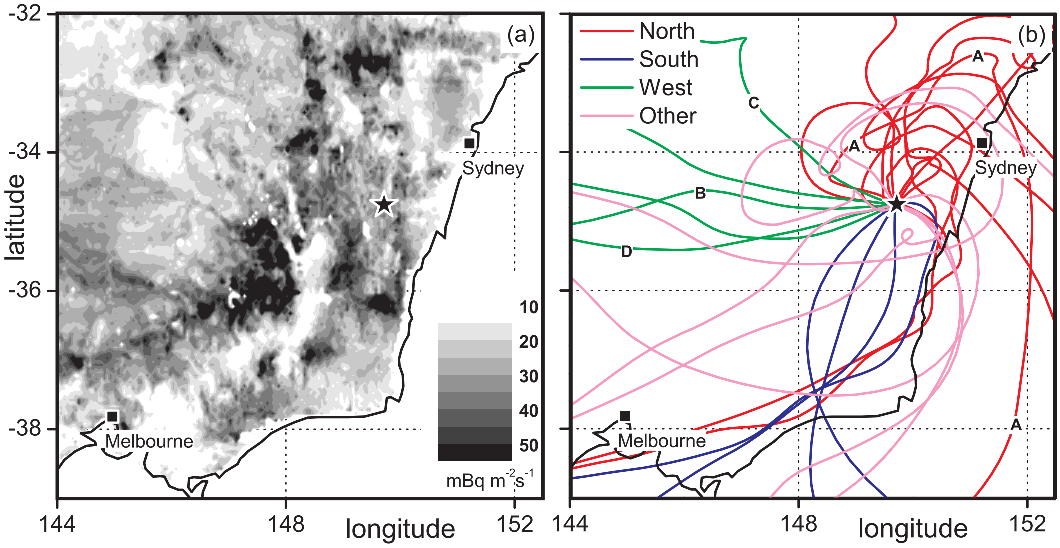

FIG. 2. (a) Radon surface flux densities (mBq m$^{-2}$ s$^{-1}$) for May 2006 (after Griffiths et al. 2010); and (b) average HYSPLIT back trajectories for each flight day, color-coded into major fetch area categories. Goulburn is marked with a black star. Marked trajectories relate to case studies CS1 (A: 14 May 2008) and CS2 (B: 20 May 2007; C: 21 May 2007; D: 22 May 2007).

cloud conditions. A wide range of stability conditions were encountered, from near-neutral to strongly convective (14 near neutral, 12 weakly convective, 9 moderately convective, and 15 strongly convective cases).

The flights have also been grouped into fetch categories (see Table B1), characterizing the geographical region traversed by the air parcel in the days prior to arrival at the field site. Inspection of Hybrid Single-Particle Lagrangian Integrated Trajectories (HYSPLITs; Draxler and Hess 1998) suggested grouping of the flights into the following four main fetch categories: north (N), south (S), west (W), and other (O). These categories are color-coded in Fig. 2, which shows (truncated) 10-day average back trajectories for each flight day. These were calculated by averaging the 6 h of trajectories preceding the final flight on each day. Also shown in Fig. 2 are estimated radon surface fluxes over southeastern Australia during May 2006 (Griffiths et al. 2010).

## 3. Results

### a. Surface time series

Important aspects of the prevailing atmospheric conditions during the Goulburn flights can be seen in the continuous time series of radon and meteorological quantities collected from the surface site during the campaigns (Fig. 3).

At night, high radon values (Fig. 3, top panel) are associated with trapping beneath a low-level nocturnal inversion (mixing suppressed by thermal stratification). During the day, on the other hand, surface radon concentrations are much smaller because of deep convective vertical mixing and are sensitive to a number of factors including ABL height (mixing depth) and venting by entrainment and cloud processes. This cycle is closely linked to the net radiation balance (Fig. 3, bottom panel), which represents the energy available to drive the surface sensible heat and moisture fluxes. The large daytime net radiation maxima in the January 2007 summer campaign, for example, generated deep boundary layers accompanied by high surface temperatures and low afternoon radon concentrations.

A strong relationship between mechanical mixing and the amplitude of the diurnal signal is evident in Fig. 3, with periods of strong wind (middle panel) associated with a much reduced diurnal cycle in both radon and air temperature (e.g., 19–22 May 2007). This relationship is illustrated most clearly in Fig. 4a, which shows diurnal radon composites for all May flights separated into two categories according to the 10-m wind speed at the time of flight. In low wind conditions ($<5$ m s$^{-1}$), a large diurnal signal results from the cycle of suppressed nighttime mixing and convective daytime mixing. In high wind speed conditions ($>5$ m s$^{-1}$), however, mechanical mixing dominates over the thermal stratification effects at night, resulting in very little diurnal variation.

Each field campaign exhibited a different baseline radon concentration (Fig. 3), corresponding to a synoptic

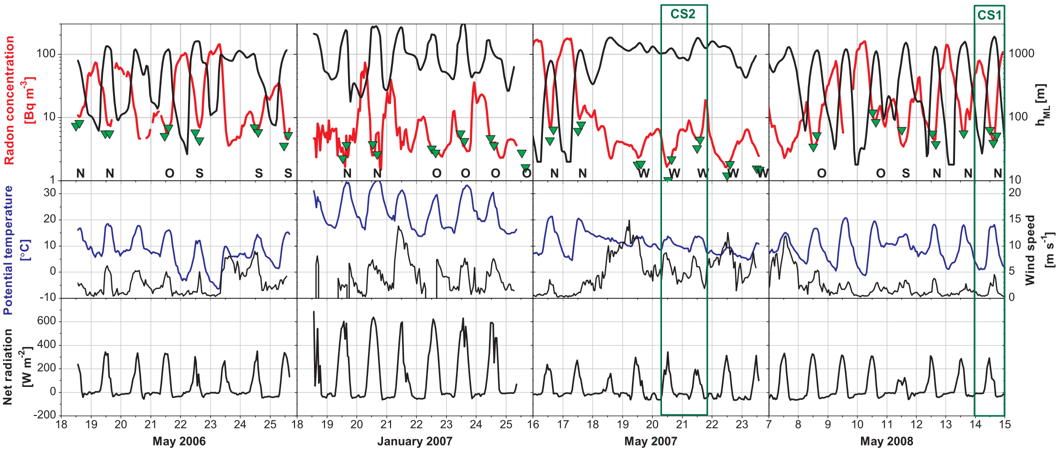

FIG. 3. Time series of radon and meteorological quantities at the surface during the Goulburn campaigns. (top) Radon at 2 m (red). Also $h_{\mathrm{ML}}$ (black) obtained from Australian Bureau of Meteorology limited area prediction system (LAPS) model (Puri et al. 1998) calibrated to agree with aircraft-derived values. Green triangles are radon concentrations from lowest (30 m) aircraft runs. Along the bottom are letters representing flight fetch categories according to Table B1. (middle) Potential temperature at 2 m (blue) and wind speed at 10 m (black). (bottom) Net radiation at 10 m. Open green boxes with labels "CS1/2" indicate case studies discussed in section 4.

"background" signal upon which the diurnal cycle is superimposed. This synoptic signal changes slowly on a time scale of days to weeks, in response to variations in the total (vertically integrated) radon content in the ABL.

### b. *Radon gradients in the daytime surface layer*

Together with the continuous surface (2 m) radon time series in the top panel of Fig. 3 are plotted radon concentrations from the lowest aircraft runs during each flight (green triangles). These measurements allow us to quantify radon gradients within the daytime atmospheric surface layer. In Fig. 5, the surface radon concentrations closest in time to each flight are compared with those from the lowest aircraft runs, separated into two categories according to the 10-m wind speed. Run-averaged aircraft altitudes were generally close to the nominal flight level of 30 m (31 ± 9 m AGL for $n = 46$ runs).

When surface radon concentrations are in the lower part of the observed range ($C_{2\mathrm{m}} = 0$–$5\ \mathrm{Bq\ m^{-3}}$), the aircraft- and surface-based data points are close in value with little scatter (Fig. 5). The average difference between the measurements, $\Delta C = C_{30\mathrm{m}} - C_{2\mathrm{m}}$, is $-0.04 \pm 0.95\ \mathrm{Bq\ m^{-3}}$ ($n = 24$) and linear least squares regression yields a best-fit line with slope 1.16 ($r^2 = 0.62$). Also shown in Fig. 5 is the average of three radon samples collected by the aircraft in a series of dedicated overpasses of the meteorological mast at 20-m altitude between 1100 and 1115 Australian eastern standard time (AEST; UTC + 10 h) 11 May 2008 (7 octas Cu/SCu; cloud types defined in footnotes of Table B1; weakly convective conditions). This overflight data, which also falls in the 0–5 $\mathrm{Bq\ m^{-3}}$ range, agrees closely with the nearest 1-h integrated data point from the surface detector ($\Delta C = 0.51 \pm 0.08\ \mathrm{Bq\ m^{-3}}$).

The lower surface concentration range ($C_{2\mathrm{m}} = 0$–$5\ \mathrm{Bq\ m^{-3}}$) corresponds to cases in which vertical mixing

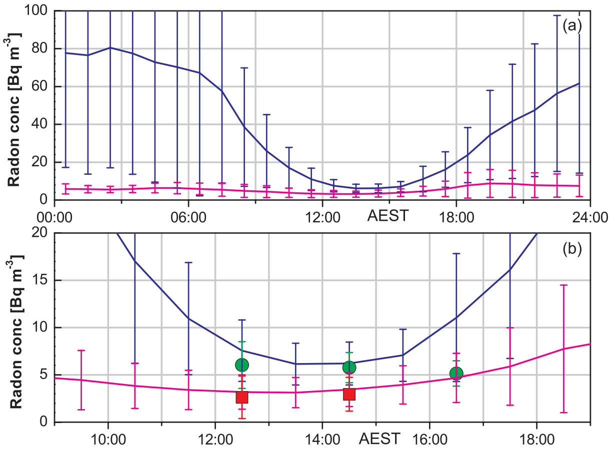

FIG. 4. Composite diurnal cycle of 2-m radon concentration for all May flights, separated into two categories according to wind speed at 10 m during the time of flight: <5 m s$^{-1}$ (blue) and >5 m s$^{-1}$ (magenta). Error bars are ±1$\sigma$ of individual diurnal cycles around the composite mean. (a) Whole diurnal cycle. (b) Midday section only. Mean of corresponding 30-m aircraft radon concentrations is shown for flights with low (green circles) and high (red squares) wind speeds, split into three groups according to the time of the lowest run in the flight: 1130–1330, 1330–1530, and 1530–1730 AEST. Error bars for these points are ±1$\sigma$ of individual flights around the group mean.

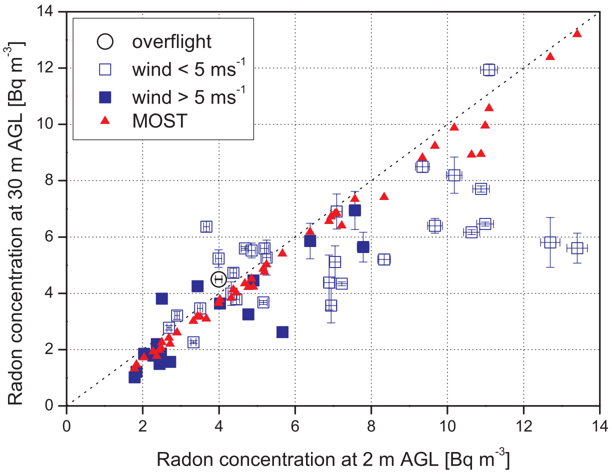

FIG. 5. Comparison between measured radon concentrations at 2 m (1-h time integration from surface detector) and 30 m (~10-km spatial integration from lowest aircraft run in each flight), split into two mechanical mixing categories according to the 10-m wind speed at the mast (open blue squares are <5 m s$^{-1}$; closed blue squares are >5 m s$^{-1}$). Red triangles are predicted radon concentrations at 30 m, calculated from the 2-m radon values using surface layer Monin–Obukhov similarity theory (MOST). Also shown is the overflight data point from 11 May 2008 (open black circle).

is strong enough to result in a negligible radon gradient between 2 and 30 m. Under such conditions, the time-integrated point measurements made at the surface (1-h average at 2-m altitude) are expected to be most comparable with the horizontally integrated aircraft measurements (10-km line average at 30-m altitude). These results therefore serve to indicate that the instrumental differences between the airborne and ground-based radon measurements are well constrained.

In the high surface concentration range ($C_{2\mathrm{m}} >$ 5 Bq m$^{-3}$), significant radon gradients are observed ($\Delta C = -2.4 \pm 2.2$ Bq m$^{-3}$ for $n = 22$) that become larger as the surface radon concentration increases (Fig. 5). For flights with surface concentrations greater than 8 Bq m$^{-3}$, radon values at 30 m appear to be independent of the surface, leveling out to around 6 Bq m$^{-3}$ with a large scatter. This higher range therefore seems to correspond to cases in which vertical mixing is becoming progressively weaker.

Also shown in Fig. 5 are predicted values for the radon concentration at the aircraft altitude, calculated from surface layer Monin–Obukhov similarity theory (MOST) using the 2-m radon measurements, surface buoyancy and momentum fluxes from the mast, and a typical surface radon flux of 23 mBq m$^{-2}$ s$^{-1}$. Commonly used versions of the Businger–Dyer formulas for the flux–gradient relationships were used (e.g., Garratt 1992, 52–54), with the assumption that the form of the integral stability-correction function for heat $\Psi_h$ is also applicable to radon. The MOST calculations predict small radon gradients for all cases ($\Delta C = -0.45 \pm 0.34$ Bq m$^{-3}$ for $n = 46$), with little scatter and no systematic differences between results in the two surface concentration ranges.

The observation that radon gradients significantly exceed similarity predictions when surface concentrations rise above a threshold supports an interpretation that MOST fails for poorly mixed conditions in which radon is ‘‘trapped’’ near the surface. The increased scatter observed in the high concentration range also supports this conclusion, as the surface- and aircraft-based measurements would be expected to become less comparable (undulating terrain is known to generate pooling and small-scale flows near the surface in weakly mixed conditions). This result clearly demonstrates the utility of the radon gradient as a sensitive and unambiguous measure of mixing strength. In contrast, the use of a low wind speed threshold to indicate poor mixing is problematic, as can be seen in Fig. 5 (many well-mixed cases occur at low wind speeds). Poorly mixed conditions near the surface in daytime are unexpected, however, and it is of interest to investigate this issue a little further.

The generation and destruction of surface layer gradients is linked to wind mixing and stability processes associated with the diurnal cycle. This is illustrated in Fig. 4b, which focuses on the daytime portion of the composite diurnal cycle presented in Fig. 4a. Averages are plotted of the 30-m aircraft radon values from the flights on the same days used for the composites, separated into three groups according to the time of the lowest run: 1130–1330, 1330–1530, and 1530–1730 AEST. For low wind speed cases, it is evident that although the surface radon time series is still dropping in the period 1130–1330 AEST, the 30-m aircraft data have reached a steady value that is maintained in the next period (1330–1530 AEST). The radon concentrations at 30 m drop later in the afternoon (1530–1730 AEST), probably due to venting from the upper layer together with the cessation of vertical transport from below, whereas the surface radon time series climbs as the new stable inversion begins to form below 30 m. It is therefore only in the central part of the afternoon (1330–1530 AEST) that conditions could be considered to be truly stationary (MOST strictly applicable), and the vertical radon gradients are always small in these cases.

### *c. Broad characteristics of the vertical radon profiles*

Appendix B documents radon concentration profiles and uncertainties for all the flights. This dataset represents a comprehensive and detailed coverage of the daytime

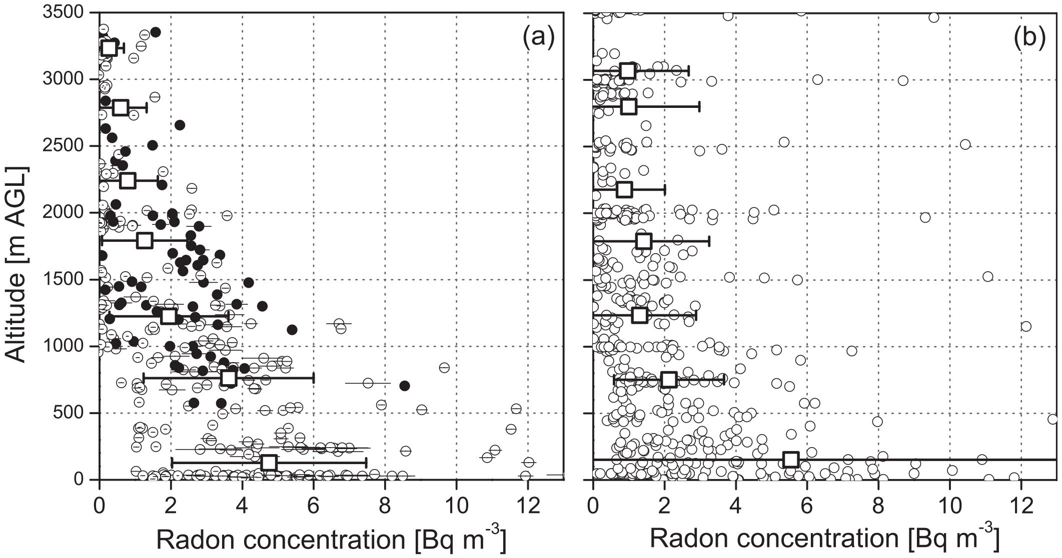

FIG. 6. (a) Scatterplot of all aircraft-sampled radon concentrations presented in this study as a function of altitude (circles), together with corresponding $\pm 1\sigma$ uncertainties (horizontal bars). Samples collected within the cloud layer are shown as closed symbols. Altitude-averaged radon concentrations, grouped into 500-m altitude bands, are also plotted as large open squares with variability indicated by $\pm 1$-$\sigma$ bars. (b) Corresponding plot using 11 inland airborne studies reported in the literature (identified in Table 1).

inland ABL under a range of conditions. To our knowledge, such a dataset is unprecedented in the published literature.

Figure 6a shows the vertical radon distribution for all measured aircraft data points, together with averages and standard deviations grouped into 500-m altitude bands. Mean radon concentrations in the lowest 1000 m (but above 30 m) of the daytime terrestrial atmosphere can range from 1 to 14 Bq m$^{-3}$ (see Table B2) but typically are around 4 ± 3 Bq m$^{-3}$. Above 1000 m, mean concentrations drop sharply to around 2 ± 2 Bq m$^{-3}$ and then slowly reduce further with height until they reach 0.3 ± 0.4 Bq m$^{-3}$ above 3000 m.

Figure 6b shows the corresponding results for 11 inland airborne studies reported in the literature (identified in Table 1). The broad description of the Goulburn dataset presented above is generally in good agreement with these previous findings, with the exception of the study by Kirichenko (1962), which reports significant radon concentrations at altitudes of 1500–4500 m AGL (contributing most of the high-radon outlying points at these altitudes in Fig. 6b). Many of the flights reported by Kirichenko were conducted in the presence of significant cumulus congestus and cumulonimbus clouds, which can rapidly transport near-surface air to high altitudes. Such conditions are not represented in the Goulburn dataset.

There is a substantial variability between individual profiles, which exhibit a range of structures in the current dataset. This variability is largely a result of vertical mixing processes of different strengths and extent, working in the ABL within the context of meteorological conditions and the recent history of the airstream. In the next three sections, we present normalized characteristics of the Goulburn profiles, grouped into three distinct boundary layer types.

### *d. Dry convective boundary layers*

The first category comprises 19 dry convective boundary layers (CBLs) listed in appendix B (Table B1). Although substantially cloud free, these cases were sometimes topped with a thin layer of inactive fair-weather cumulus or stratocumulus.

Figure 7a shows all the aircraft radon data for the flights in this category, normalized with corresponding near-surface (30 m) radon concentrations $C_{\mathrm{sfce}}$ and mixed layer depths (Table B1). In all cases, there is a very marked drop in concentrations from high values within the (surface coupled) mixed layer to near-zero values in the free troposphere above. This occurs under a range of conditions, from light-wind strong convection to high-wind near-neutral boundary layers.

In the presence of this large change at the capping inversion, the ‘‘top-down’’ diffusion process associated with entrainment through the interface leads to a range of radon gradients in the upper part of the mixed layer (Fig. 7a) despite uniform potential temperature profiles (Fig. 7b). Top-down diffusion of scalars in convectively

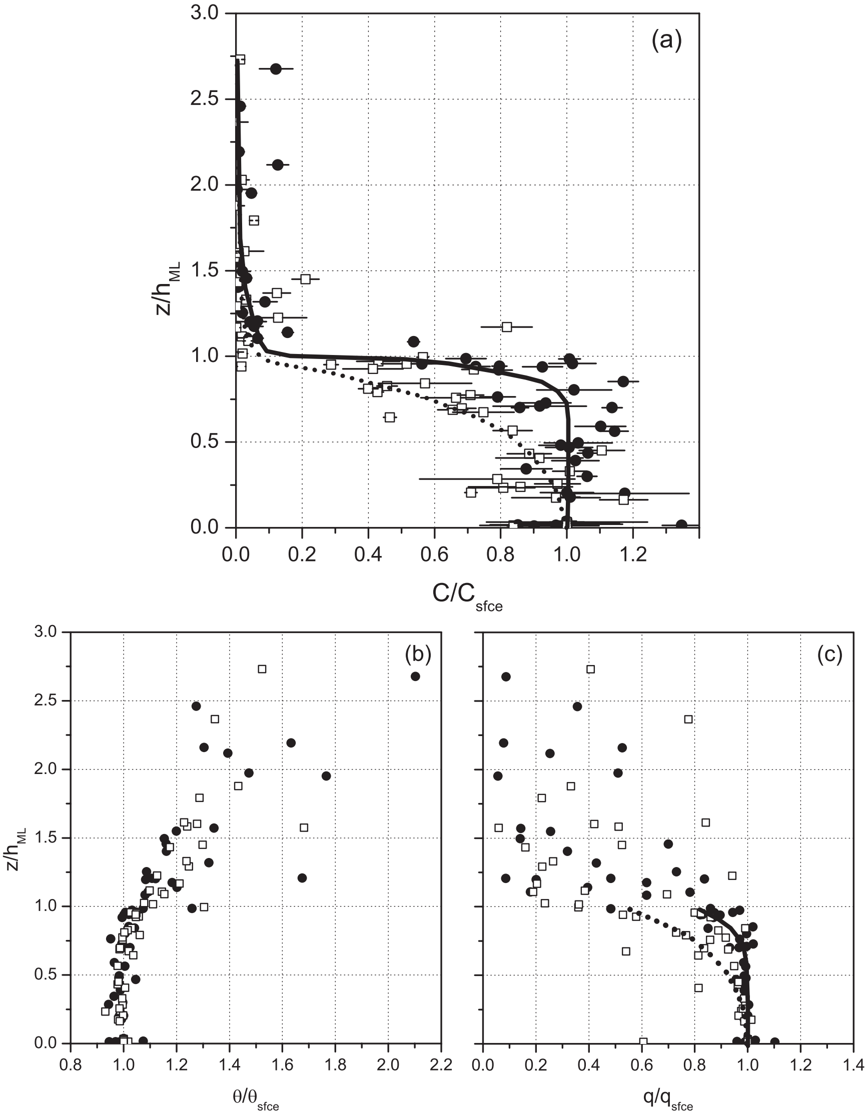

FIG. 7. Profiles of (a) radon concentration $C$, (b) potential temperature $\theta$, and (c) specific humidity $q$ from 19 dry convective boundary layers sampled during the Goulburn aircraft campaigns (Table B1). Abscissas are normalized with near-surface (30 m) values from individual flights ($C_{\mathrm{sfce}}$, $\theta_{\mathrm{sfce}}$, $q_{\mathrm{sfce}}$); ordinates are $z$ normalized with $h_{\mathrm{ML}}$ (Table B1). Open squares indicate nine cases chosen as having large radon gradients: M6F03, M6F06, M6F07, M6F12, J7F12, M7F10, M7F13, M8F03, and M8F08. Solid circles correspond to the other 10 cases. Solid (small gradient) and dotted (large gradient) lines are drawn to guide the eye.

mixed boundary layers was first investigated by Wyngaard and Brost (1984) and Moeng and Wyngaard (1984). These studies derived theoretical scalar concentration profiles for a range of entrainment rates and concluded in particular that strong entrainment leads to the characteristic profiles with significant gradients in the upper mixed layer that are sometimes observed in ABL humidity soundings (e.g., Mahrt 1976).

To further investigate these effects with the present dataset, nine of the dry CBL flights were chosen by inspection as having large radon gradients in the upper part of the mixed layer: M6F03, M6F06, M6F07, M6F12, J7F12, M7F10, M7F13, M8F03, and M8F08 (Table B1). These flights are marked with open squares in Fig. 7a and also in Figs. 7b and 7c, which show normalized potential temperature and specific humidity profiles for the Goulburn dry CBL cases.

It can be seen in Fig. 7c that the flights exhibiting large radon gradients within the mixed layer also tend to exhibit large humidity gradients. However, the curvature

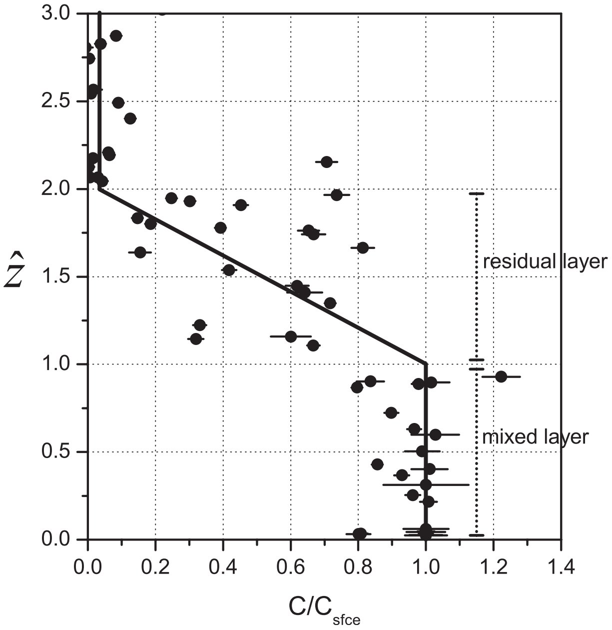

FIG. 8. Profiles of $C$ from 10 mixed layers topped with residual layers sampled during the Goulburn campaigns (Table B1). Abscissa is normalized with near-surface (30 m) values from individual flights $C_{\mathrm{sfce}}$; ordinate is a hybrid normalized altitude $\hat{z}$, scaled so that the mixed layer falls in the range 0–1 and the residual layer falls in the range 1–2 (see text for definition of $\hat{z}$). Solid line is drawn to guide the eye.

of the humidity profiles in these cases is less pronounced than it is for radon, and the curved portion occupies a smaller fraction of the mixed layer (top 25%, compared with 50% for radon). These differences result mainly from the fact that the change in humidity across the capping inversion is smaller than the corresponding change in radon concentrations. In fact, a large range of values and profile shapes is encountered above the top of the mixed layer in the humidity signal (Fig. 7c).

### e. *Mixed layers topped with residual layers*

Residual layers represent the remains of the previous day's boundary layer, after the convective turbulence has subsided. Although the lower part of the residual layer is eroded by the stable boundary layer overnight, the upper part remains nonturbulent and retains the scalar structure from the previous afternoon until it is eventually replaced by the following morning's growing convective mixed layer (Stull 1988, 14–15).

Ten of the boundary layers listed in Table B1 consisted of shallow mixed layers topped with residual layers extending to a capping inversion. These profiles are plotted together in Fig. 8, with an altitude (ordinate) axis scaled so that the mixed layer falls in the range 0–1 and the residual layer falls in the range 1–2:

$$\hat{z} = \begin{cases} \dfrac{z}{h_{\mathrm{ML}}}, & z \le h_{\mathrm{ML}} \\ 1 + \dfrac{z - h_{\mathrm{ML}}}{h_{\mathrm{RL}} - h_{\mathrm{ML}}}, & h_{\mathrm{ML}} < z \le h_{\mathrm{RL}} \\ 1 + \dfrac{z}{h_{\mathrm{RL}}}, & z > h_{\mathrm{RL}} \end{cases}.$$

Radon exhibits a fairly constant profile in the mixed layer, probably on account of vigorous turbulent mixing that is growing upward into the residual layer. The strong radon gradients seen in the upper mixed layer of the fully developed CBL cases are not apparent here, as there is no sharp change in radon concentration across the top of the mixed layer.

In the residual layer, radon concentrations are quite variable but on average tend to reduce linearly with height. These observations are consistent with the fact that the residual layer constitutes the remnants of the previous day's ABL, decayed overnight. The variability may result from horizontal advection effects that change with height in the absence of vertical mixing.

In the free atmosphere above the capping inversion ($\hat{z} > 2$), radon concentrations are again very small as compared with near-surface values.

### f. *Coupled cloud layers*

Figure 9 shows radon profiles for 21 convective boundary layers topped with substantial coupled nonprecipitating cloud layers (listed in Table B1). These include some dissipated cloud layers; that is, active clouds had been present in the preceding hours but few were left by the time of the flight. Open squares in Fig. 9 indicate nine cases in which the cloud-base wind speed was high ($>8.5$ m s$^{-1}$): M6F10, M6F11, J7F03, M7F05, M7F06, M7F07, M7F11, M7F12, and M7F14. The altitude (ordinate) axis is scaled so that the subcloud layer falls in the range 0–1 and the cloud layer falls in the range 1–2 (i.e., $\hat{z}$ is defined analogously to the residual layer scaling in section 3e).

The lack of a discontinuity in the radon profiles at cloud base ($\hat{z} = 1$) confirms that the subcloud and cloud layers are coupled in the chosen cases. Significant radon concentrations are present throughout both layers, generally reducing with increasing altitude as the subcloud- and cloud-layer air mix. In the undisturbed free atmosphere above cloud top ($\hat{z} > 2$), radon concentrations are again very small as compared with near-surface values.

The radon concentration in the subcloud layer reduces roughly linearly with height to reach concentrations of approximately $0.5C_{\mathrm{sfce}}$ at cloud base. This indicates a two-endpoint mixing behavior, consistent with the dynamics of ''cloud root'' circulations in the

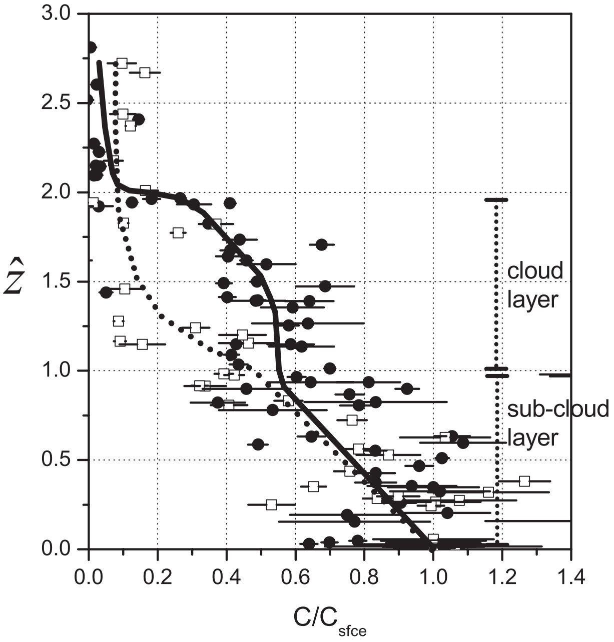

FIG. 9. Profiles of $C$ from 21 convective boundary layers topped with coupled nonprecipitating clouds sampled during the Goulburn campaigns (Table B1). Abscissa is normalized with $C_{\mathrm{sfce}}$; ordinate is $\hat{z}$, scaled so that the subcloud layer falls in the range 0–1 and the cloud layer falls in the range 1–2 (see text for definition of $\hat{z}$). Open squares indicate 9 cases where cloud-base ($\hat{z} = 1$) wind speed exceeds 8.5 m s$^{-1}$: M6F10, M6F11, J7F03, M7F05, M7F06, M7F07, M7F11, M7F12, and M7F14. Solid circles correspond to the other 12 cases. Solid (low wind) and dotted (high wind) lines are drawn to guide the eye.

subcloud layer (LeMone and Pennell 1976; Nicholls and LeMone 1980; Stull 1985; Ötles and Young 1996). Radon-rich air from near the surface is mixed upward into the bases of detraining clouds, and radon-depleted intercloud air is mixed downward into the subcloud layer by intercloud downdrafts.

In the cloud layer, the radon profile for low and moderate wind speeds is constant with altitude in the range of $\hat{z} = 1.0-1.5$ and then drops off to reach free atmospheric values above cloud top. As the aircraft did not fly inside the clouds, the measured radon concentrations are indicative of the intercloud spaces and the air at the edges of clouds. The cloud layer profiles therefore measure the extent to which air is being detrained out of the clouds in a boundary layer venting process.

In high-wind-speed cases (>8.5 m s$^{-1}$; open squares in Fig. 9), the radon distributions do not exhibit the ‘‘bulge’’ (constant portion) in the lower half of the cloud layer. This may indicate that high-wind-speed (near neutral) conditions tend to inhibit the vertical transport of radon within clouds.

## 4. Case studies

To illustrate the relationship between diurnal/synoptic forcings and the evolution of vertical radon distributions in the ABL, we present below two sequences of aircraft profiles collected under markedly different meteorological conditions.

### a. *Case study 1: Diurnal evolution of a cumulus-topped CBL in light winds*

Figure 10 presents three consecutive flights conducted on a single day (14 May 2008; marked ‘‘A’’ in Fig. 2 and ‘‘CS1’’ in Fig. 3) characterized by light northerly winds and large diurnal variations in radon, air temperature, and ABL depth.

The early morning was characterized by light winds and fog patches. The fog dispersed by the time of the first flight, however, and skies were clear apart from a few small altocumuli (Fig. 10a, left panel). The 2-m radon values reached a peak of around 80 Bq m$^{-3}$ the previous night (Fig. 10b), indicating that a stable boundary layer (SBL) had developed close to the ground. A pronounced temperature inversion adjacent to the surface, evident in the initial (climbing) aircraft sounding, was destroyed by surface heating during the first flight (Fig. 10c, left panel). By the end of the descending stack pattern, this inversion had been replaced by an adiabatic layer with a potential temperature indistinguishable from that of the deep residual layer above.

Despite the uniform temperature profile, however, the radon vertical profile indicates that the top of the developing mixing layer (marked ‘‘ML’’ in Fig. 10c, left panel) had not yet reached the capping inversion (marked ‘‘RL’’). In fact, ML was still at an altitude less than half that of RL, as is clearly shown by a steep radon gradient in the altitude band 550–850 m AGL. Farther up, the radon profile is relatively constant with height (~3 Bq m$^{-3}$) within the residual layer and only drops to background values above the capping inversion.

By the end of the first flight, fair-weather cumulus clouds were starting to appear. These developed rapidly, and the boundary layer during the second (early afternoon) flight was topped with a cloud deck of 4 octas of moderately developed nonprecipitating cumulus with a depth of up to 1000 m (Fig. 10a, middle panel). The surface radon time series reached a minimum during this time (Fig. 10b), and the radon concentrations in the subcloud layer were similar in magnitude to the surface and uniformly distributed almost up to cloud base (Fig. 10c, middle panel). Radon concentrations in the cloud layer above, although smaller, remained significant all the way to cloud top, which extended well above the top of the previous residual layer. It therefore seems

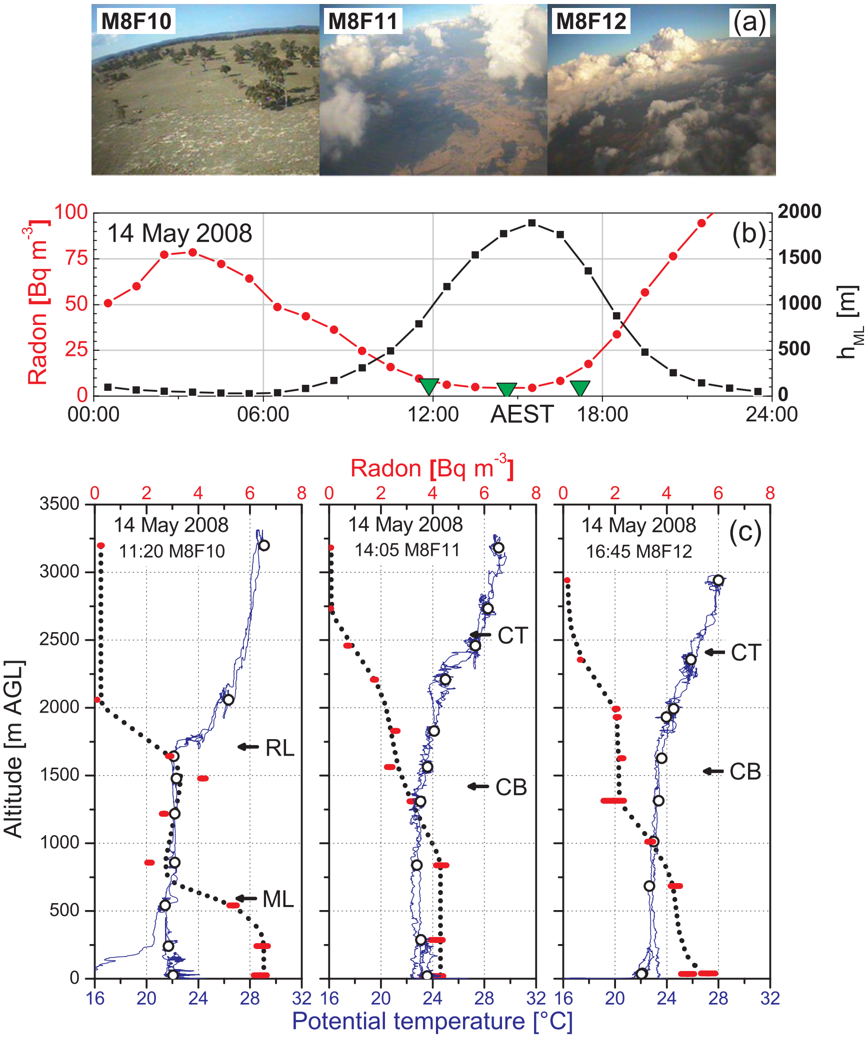

FIG. 10. Case study 1 (diurnal evolution of a cumulus-topped CBL in light winds). Three radon profiles flown on 14 May 2008. (a) Pod-camera photos indicating weather conditions. (b) Time series of radon at 2 m (red lines), lowest aircraft runs (large green triangles), and mixed layer height (black lines). (c) Radon (red bars: length indicates uncertainty; dotted black lines, drawn to guide the eye) and $\theta$ (blue lines) profiles. Black circles are averages of the (1 Hz) $\theta$ data over the radon sampling periods. Tops of the mixed layer (ML) and residual layer (RL) and cloud base (CB) and cloud top (CT) heights are also marked (see Table B1).

clear that the clouds were acting as an enhanced venting mechanism for radon from the subcloud layer.

The third flight, in the late afternoon, was flown in conditions of weakening convection and a decaying cloud layer that had reduced to 2 octas of isolated cumulus patches (Fig. 10a, right panel). Radon levels in the cloud layer were similar to the previous flight, but in the subcloud layer a pronounced vertical radon gradient had developed (Fig. 10c, right panel). This is likely to be a consequence of downward mixing of radon-depleted air associated with cloud motions into the upper subcloud layer, together with a weakening of the upward transport of near-surface air by convection as the surface heating diminished. Near the surface, a new stable boundary layer was forming, evidenced by increasing radon concentrations and decreasing temperatures close to the ground. In the 2-m time series data (Fig. 10b), radon concentrations were already increasing during the time of the final flight.

### b. *Case study 2: Strong-wind neutral boundary layer and transition*

In the May 2007 campaign, high wind speed conditions persisted for 6 days during a prolonged period of

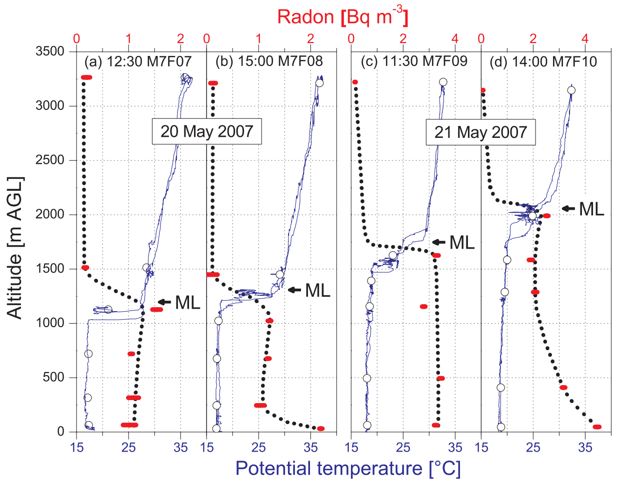

FIG. 11. Case study 2 (strong-wind neutral boundary layer and transition). Four radon profiles flown on 20–21 May 2007. Radon (red bars: length indicates uncertainty; dotted black lines, drawn to guide the eye) and $\theta$ (blue lines) profiles. Black circles are averages of the (1 Hz) $\theta$ data over the radon sampling periods. Top of the mixed layer (ML) is also marked (see Table B1). Note change of radon scale between left and right pairs of panels.

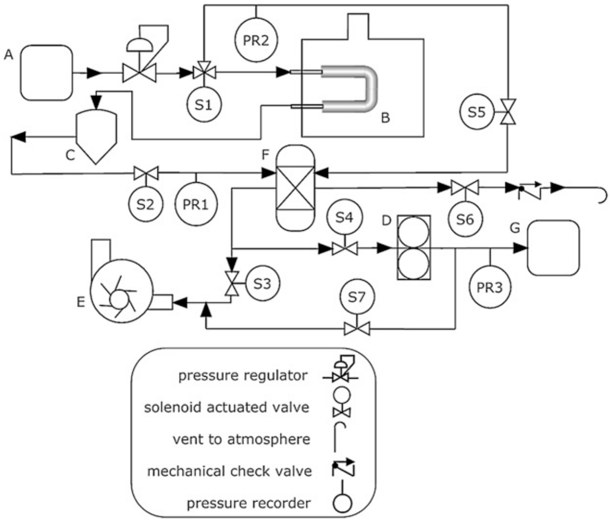

FIG. A1. Radon extraction rig at the Lucas Heights flight support laboratory. Major labeled components: A, conditioned nitrogen; B, sampling tube inside electric oven; C, water scrubber; D, peristaltic pump; E, vacuum pump; F, radon collection trap; and G, Lucas scintillation cell.

westerly flow across inland Australia (Fig. 3). A near-neutral boundary layer was established that remained deep and well mixed throughout the period, and the surface time series of radon and air temperature exhibited only small diurnal variations (Fig. 3).

Figure 11 presents a sequence of four flights conducted over 2 days (20–21 May 2007) during the central part of this episode, labeled "B" and "C" in Fig. 2 and "CS2" in Fig. 3. A shallow layer of cloud (4–6 octas of mixed Cu/SCu) capped the mixed layer but was not vertically active.

The two flights on the first day (20 May 2007), 3 h apart, revealed similar mixed layer depths and vertical profiles (Figs. 11a,b). Radon and potential temperature were constant with height within the mixed layer and exhibited large jumps across the capping inversion. The ABL was therefore in a well-mixed quasi-equilibrium state during these flights, with a near-zero surface heat flux and little or no entrainment.

By late morning the next day (21 May 2007), radon concentrations in the mixed layer had increased by approximately 2 Bq m$^{-3}$ and the mixed layer top had risen by 200–300 m (Fig. 11c). The profile shape remained essentially constant with height through the mixed layer, indicating that entrainment effects were still small compared with the efficiency of wind-driven mixing. Only about half of the change in total ABL radon content (estimated by vertical integration of the profiles) over the intervening 21-h period was accounted for by a simple calculation using estimated surface radon emissions, however. The remaining portion is likely to be due to advective influences, as airflow trajectories changed significantly overnight, from westerly to northwesterly (Fig. 2, marked "B" and "C").

By the time of the final flight in the sequence, 2 h later, the mixed layer top had risen another 500 m (Fig. 11d). Entrainment of radon-free air from above had significantly reduced concentrations in the upper mixed layer, resulting in a strong radon gradient. Wind speeds dropped, leading to a moderate buildup of radon close to the surface. The next day (22 May 2007; not shown), wind speeds picked up and turned westerly again (Fig. 2, marked "D"); the neutral boundary layer was reestablished and radon concentrations dropped back to low values (Fig. 3).

The striking contrast between the radon profiles in this (wind shear driven) neutral boundary layer and the (surface heating driven) CBL discussed in the previous case study demonstrates well the utility of radon profiling as a tool for quantitative analysis of boundary layer mixing processes.

## 5. Summary and conclusions

We have presented and discussed features of a unique dataset of high-resolution vertical profiles of radon in clear and cloudy daytime terrestrial boundary layers over simple terrain. Fifty radon profiles, extending from the surface to 3.5 km AGL, were obtained over a period of 2 yr using a sampling system based on charcoal traps

TABLE B1. Flight times, naming conventions, layer depths, clouds, and categorization for the Goulburn campaigns. Flight ID (column 2) format is MYFNN, where MY is the month and year of the campaign (M = "M" for May, "J" for January; Y = last digit of year 200Y) and NN is the 2-digit flight number.

| Time[a] and date | Flight ID | $h_{\mathrm{ML}}/h_{\mathrm{CB}}$ (m AGL)[b] | $h_{\mathrm{CT}}/h_{\mathrm{RL}}$ (m AGL)[b] | Cloud fraction (octas) | Cloud/RL[c] | Additional comments[c] | Category BL/stab/fetch[d] |
|---|---|---|---|---|---|---|---|
| May 2006 | | | | | | | |
| 1552 AEST 17 May | M6F01 | 750 | 1200 | 0 | —/RL | — | R/0/N |
| 1204 AEST 18 May | M6F02 | 900 | — | 0 | — | Hazy; cirrus | B/2/N |
| 1521 AEST 18 May | M6F03 | 1000 | — | 0 | — | Hazy; cirrus | B/3/N |
| 1215 AEST 19 May | M6F04 | 700 | 2000 | 3 | Cu | Cu advecting over flight region | C/1/N |
| 1507 AEST 19 May | M6F05 | 700 | 2000 | 5 | Cu | Cu weakening | C/1/N |
| 1146 AEST 21 May | M6F06 | 1000 | — | 0 | — | — | B/3/O |
| 1454 AEST 21 May | M6F07 | 1200 | — | 0 | — | — | B/2/O |
| 1234 AEST 22 May | M6F08 | 900 | 3000 | 6 | Cu | — | C/3/S |
| 1547 AEST 22 May | M6F09 | 1500 | 3000 | 6 | Cu | — | C/2/S |
| 1215 AEST 24 May | M6F10 | 900 | 2000 | 6 | SCu | Windy | C/0/S |
| 1459 AEST 24 May | M6F11 | 750 | 2000 | 5 | SCu | Windy | C/0/S |
| 1155 AEST 25 May | M6F12 | 800 | — | 0 | — | A few cirrus | B/2/S |
| 1502 AEST 25 May | M6F13 | 1200 | 1200 | 0.5 | Cu | A few cirrus | B/2/S |
| Jan 2007 | | | | | | | |
| 1215 AEDT 19 Jan | J7F01 | 1100 | 2000 | 0 | —/RL | Hazy; a few cirrus | R/3/N |
| 1518 AEDT 19 Jan | J7F02 | 2200 | 4000 | 3.5 | Cu | Hazy and hot; $h_{\mathrm{CT}}$ guess only | C/3/N |
| 1225 AEDT 20 Jan | J7F03 | 2200 | 3500 | 0.5 | Cu | Cu developing | B/1/N |
| 1550 AEDT 20 Jan | J7F04 | 3000 | 3500 | 1.5 | Cu | Cu weakening | B/1/N |
| 1150 AEDT 22 Jan | J7F05 | 1500 | 2000 | 2.5 | Cu | Cu weakening | B/3/O |
| 1447 AEDT 22 Jan | J7F06 | 2100 | 2500 | 0.5 | Cu | Cu almost gone | B/3/O |
| 1054 AEDT 23 Jan | J7F07 | 750 | 1900 | 0 | —/RL | Hazy | R/3/O |
| 1402 AEDT 23 Jan | J7F08 | 2200 | 3500 | 2.5 | Cu | $h_{\mathrm{CT}}$ guess only | C/1/O |
| 1102 AEDT 24 Jan | J7F09 | 1400 | 1800 | 5 | Cu + SCu | Cu developing through SCu | C/2/O |
| 1351 AEDT 24 Jan | J7F10 | 1900 | 2800 | 5.5 | Cu | Cu developing strongly | C/1/O |
| 1213 AEDT 25 Jan | J7F11 | 1200 | 1800 | 0.5 | Cu/RL | Cu almost gone | R/2/O |
| 1500 AEDT 25 Jan | J7F12 | 2250 | — | 0 | — | — | B/3/O |
| May 2007 | | | | | | | |
| 1322 AEST 16 May | M7F01 | 750 | 1350 | 0 | —/RL | Layers hard to define; 7/8 altostratus | R/1/N |
| 1606 AEST 16 May | M7F02 | 600 | 1300 | 0 | —/RL | ML/RL hard to define; 4/8 altostratus | R/1/N |
| 1154 AEST 17 May | M7F03 | 900 | 1600 | 0 | —/RL | Two higher inversions; thin cirrostratus | R/3/N |
| 1435 AEST 17 May | M7F04 | 1100 | 3000 | 5 | Cu | Line of Cu; overcast cirrostratus | C/3/N |
| 1151 AEST 19 May | M7F05 | 1250 | 2300 | 6 | Cu + SCu | Cu advected in overnight | C/0/W |
| 1429 AEST 19 May | M7F06 | 1550 | 2200 | 5 | Cu + SCu | Cu weakening | C/0/W |
| 1222 AEST 20 May | M7F07 | 1150 | 1500 | 5 | Cu + SCu | Cu weakening | C/0/W |
| 1456 AEST 20 May | M7F08 | 1200 | 1500 | 4 | SCu | Thin SCu layer | B/0/W |
| 1137 AEST 21 May | M7F09 | 1650 | 2000 | 6 | Cu | Thin inactive Cu; a few altostratus | B/0/W |
| 1357 AEST 21 May | M7F10 | 2000 | 2200 | 6 | Cu | Thin inactive Cu; a few altostratus | B/0/W |
| 1145 AEST 22 May | M7F11 | 1300 | 1900 | 4 | Cu | Ragged Cu | C/0/W |
| 1402 AEST 22 May | M7F12 | 1100 | 1800 | 3 | Cu | Ragged Cu | C/0/W |
| 1143 AEST 23 May | M7F13 | 750 | 900 | 3 | Cu + SCu | Thin patchy Cu | B/0/W |
| 1358 AEST 23 May | M7F14 | 900 | 1400 | 4 | Cu + SCu | Patchy Cu | C/0/W |

TABLE B1. (*Continued*)

| | | | | | | | |
|---|---|---|---|---|---|---|---|
| May 2008[e] | | | | | | | |
| 1145 AEST 8 May | M8F02 | 900 | — | 0 | — | Light winds | B/2/O |
| 1431 AEST 8 May | M8F03 | 1200 | — | 0 | — | Light winds | B/1/O |
| 1159 AEST 10 May | M8F04 | 600 | 900 | 0 | —/RL | Light winds | R/3/O |
| 1443 AEST 10 May | M8F05 | 1200 | 1500 | 1.5 | Cu | Light winds | B/1/O |
| 1141 AEST 11 May | M8F06 | 500 | 1350 | 7 | Cu + SCu | Light winds | C/1/S |
| 1238 AEST 12 May | M8F07 | 350 | 850 | 1 | SCu/RL | Patchy SCu; light winds | R/1/N |
| 1520 AEST 12 May | M8F08 | 1650 | 1900 | 3 | Cu | Light winds | B/2/N |
| 1357 AEST 13 May | M8F09 | 1350 | 2000 | 2 | Cu | Light winds; clouds building up; a few cirrus | C/3/N |
| 1120 AEST 14 May | M8F10 | 600 | 1750 | 0 | —/RL | Light winds | R/3/N |
| 1406 AEST 14 May | M8F11 | 1400 | 2500 | 4 | Cu | Light winds | C/3/N |
| 1647 AEST 14 May | M8F12 | 1600 | 2400 | 2 | Cu | Light winds; clouds weakening | C/0/N |

[a] Midtime of vertical radon stack in Australian eastern standard time (AEST; UTC + 10 h) or eastern daylight time (AEDT; UTC + 11 h).

[b] The variables $h_{\mathrm{ML}}$, $h_{\mathrm{RL}}$, $h_{\mathrm{CB}}$, and $h_{\mathrm{CT}}$ are altitudes (m AGL) of mixed and residual layer top and cloud base and top, respectively, derived from aircraft ascents and observations.

[c] RL: residual layer; Cu: cumulus; SCu: stratocumulus (all nonprecipitating).

[d] BL: boundary layer, where B is blue sky (few or no clouds), R is residual layer, and C is substantial active clouds; stab is stability, where 0 is near neutral ($-h_{\mathrm{ML}}/L < 10$), 1 is weakly convective ($10 \leq h_{\mathrm{ML}}/L < 50$), 2 is moderately convective ($50 \leq h_{\mathrm{ML}}/L < 100$), and 3 is strongly convective ($-h_{\mathrm{ML}}/L \geq 100$); and fetch indicates direction, where N is north, S is south, W is west, and O is other.

[e] Flight M8F01 is not shown, because it produced no radon profile.

mounted on an instrumented motorized research glider. Conditions ranged from neutral to strongly convective and from clear skies to coupled nonprecipitating cumulus.

Mean radon concentrations encountered in the aircraft data are typically 4 ± 3 Bq $\mathrm{m}^{-3}$ in the lowest 30–1000 m of the daytime atmosphere, although they can range from 1 to 14 Bq $\mathrm{m}^{-3}$ (Table B2). Above 1000 m, radon concentrations drop sharply to around 2 ± 2 Bq $\mathrm{m}^{-3}$ and then steadily reduce further with height until they reach 0.3 ± 0.4 Bq $\mathrm{m}^{-3}$ above 3000 m in this dataset. Individual vertical radon profiles exhibit a substantial variability, resulting mainly from vertical mixing processes of different strengths and extent, working in the ABL within the context of ambient meteorological conditions and the recent history of the airstream.

Normalized aircraft radon measurements reveal the characteristic structure and variability of three major classes of daytime boundary layer:

1) *Dry convective boundary layers.* Measured radon profiles display a large range of gradients in the upper mixed layer, due to ‘‘top-down’’ diffusion processes. As a consequence of the large concentration change consistently present across the mixed layer top, radon is a highly sensitive and unambiguous indicator of entrainment.
2) *Mixed layers topped with residual layers.* Radon exhibits a constant profile within the growing morning mixed layer. In the residual layer, radon profiles are variable but tend to reduce linearly with height to reach negligible levels above the capping inversion. Variability in the profiles may result from horizontal advection effects occurring overnight in the absence of mixing.
3) *Convective boundary layers topped with coupled nonprecipitating clouds.* Radon concentrations reduce roughly linearly with height in the subcloud layer, indicating a mixing behavior consistent with ‘‘cloud root’’ circulations. The radon profile is fairly constant through the lower part of the cloud layer but then drops off toward cloud top. The cloud layer profiles reflect the extent to which air is detrained out of the clouds into the intercloud spaces. There is some evidence to indicate that high wind speed (near neutral) conditions may tend to inhibit the vertical venting of radon by cloud motions.

In poorly mixed conditions, radon gradients in the daytime atmospheric surface layer significantly exceed those predicted by Monin–Obukhov similarity theory (MOST). Our results demonstrate the utility of the radon gradient as an indicator of conditions under which MOST may be expected to fail. Generation and destruction of surface layer gradients, and the shape of the lower part of the aircraft profiles, are linked closely to the diurnal processes of formation and erosion of the nocturnal stable boundary layer. Higher up, the shape of radon profiles in the residual layer is substantially a

TABLE B2. Aircraft radon profiles from Goulburn campaigns. Flight ID (column 1) format is as in Table B1. For each flight, three rows of numbers characterize the measured profile: $Z$ is altitude (m AGL), $C$ is radon concentration in (mBq m$^{-3}$), and $E$ is radon uncertainty (mBq m$^{-3}$). The asterisk for the three data points during M8F06 indicates flights directly over the surface radon detector at 20-m altitude.

| | | | | | | | |
|---|---|---|---|---|---|---|---|
| May 2006 | | | | | | | |
| M6F01 | *Z* | 36.2 | 233.7 | 1036.8 | 821.3 | 1278.9 | 1879.1 |
| | *C* | 13 121 | 6219 | 961 | 3733 | 37 | 103 |
| | *E* | 592 | 553 | 182 | 162 | 147 | 157 |
| M6F02 | *Z* | 257.3 | 27.7 | 1057.3 | 723.6 | 888.4 | 1905.7 |
| | *C* | 14 393 | 7360 | 402 | 7521 | 5115 | 929 |
| | *E* | 713 | 528 | 196 | 634 | 255 | 230 |
| M6F03 | *Z* | 29.3 | 233.0 | 970 | 1170 | 1370 | 2030 |
| | *C* | 8194 | 6617 | 3523 | 6706 | 1011 | 140 |
| | *E* | 641 | 589 | 458 | 348 | 327 | 188 |
| M6F04 | *Z* | 31.5 | 227.2 | 1161.6 | 1913.6 | 1479.7 | 1315.2 |
| | *C* | 5603 | 5709 | 3311 | 1714 | — | 3843 |
| | *E* | 530 | 608 | 405 | 230 | — | 304 |
| M6F05 | *Z* | 26.6 | 242.8 | 248.0 | 876.7 | 1477.8 | 3032.9 |
| | *C* | — | 5641 | 5289 | 3483 | 2911 | 0 |
| | *E* | — | 527 | 536 | 424 | 392 | 91 |
| M6F06 | *Z* | 25.6 | 238.8 | 926.7 | 1292.5 | 1107.0 | 1877.9 |
| | *C* | 5115 | 4397 | 2117 | 9 | 0 | 0 |
| | *E* | 574 | 635 | 399 | 247 | 423 | 144 |
| M6F07 | *Z* | 34.7 | 211.2 | 911.0 | 1340.6 | 1147.6 | 1899.2 |
| | *C* | 6905 | 6677 | 4592 | 118 | 3564 | 6 |
| | *E* | 620 | 706 | 608 | 315 | 425 | 140 |
| M6F08 | *Z* | 25.5 | 173. 7 | 841.3 | 808.4 | 1722.6 | 2837.9 |
| | *C* | 5808 | 4352 | 3739 | 2660 | 2815 | 171 |
| | *E* | 887 | 691 | 451 | 622 | 259 | 235 |
| M6F09 | *Z* | 22.7 | 232.2 | 1167.9 | 1236.9 | 1897.6 | 236.6 |
| | *C* | 4381 | 3380 | 2340 | 3646 | 2785 | 6554 |
| | *E* | 975 | 599 | 445 | 403 | 346 | 395 |
| M6F10 | *Z* | 31.6 | 238.3 | 822.8 | 1580.0 | 2354 | 224.1 |
| | *C* | 6945 | 6994 | 2344 | 0 | 498 | 3686 |
| | *E* | 675 | 594 | 353 | 413 | 186 | 309 |
| M6F11 | *Z* | 35.2 | 239.4 | 943.8 | 1001.5 | 1324.1 | 1927.4 |
| | *C* | 5857 | 6793 | 2712 | 2616 | 611 | 75 |
| | *E* | 630 | 723 | 405 | 280 | 297 | 160 |
| M6F12 | *Z* | 26.8 | 228.1 | 674.7 | 1290.9 | 980.9 | 1892.7 |
| | *C* | 3565 | 2815 | 2036 | 91 | 453 | 0 |
| | *E* | 613 | 684 | 362 | 208 | 298 | 146 |
| M6F13 | *Z* | 25.9 | 240.4 | 851.7 | 1443.5 | 1167.7 | 2367.8 |
| | *C* | 5269 | 6186 | 4835 | 221 | 0 | 19 |
| | *E* | 625 | 721 | 473 | 261 | 0 | 170 |
| January 2007 | | | | | | | |
| J7F01 | *Z* | 34.4 | 2307.9 | 1697 | 1021.8 | 553.4 | 29.7 |
| | *C* | 2013 | 1776 | 2044 | 3074 | 2487 | 2514 |
| | *E* | 56 | 50 | 47 | 91 | 97 | 86 |
| J7F02 | *Z* | 32 | 3353.5 | 2655.8 | 1978 | 1028.6 | 33.9 |
| | *C* | 3482 | 1563 | 2246 | 3576 | 3712 | 3870 |
| | *E* | 95 | 126 | 94 | 92 | 122 | 104 |
| J7F03 | *Z* | 30.1 | 3289.3 | 2632.4 | 2021.9 | 1057.7 | 30.4 |
| | *C* | 4371 | 64 | 166 | 2579 | 3186 | 3247 |
| | *E* | 108 | 77 | 42 | 97 | 182 | 115 |
| J7F04 | *Z* | 34 | 3321.9 | 2867.6 | 2183.8 | 1173.8 | 35.6 |
| | *C* | 2484 | 92 | 1551 | 2581 | 2829 | 2758 |
| | *E* | 144 | 43 | 144 | 117 | 35 | 189 |

TABLE B2. (*Continued*)

| | | | | | | | |
|---|---|---|---|---|---|---|---|
| January 2007 | | | | | | | |
| J7F05 | *Z* | 27.3 | 3289.1 | 1977.4 | 1436.6 | 702.3 | 27.4 |
| | *C* | 3470 | 30 | 307 | 3528 | 3493 | 2957 |
| | *E* | 173 | 44 | 125 | 99 | 101 | 224 |
| J7F06 | *Z* | 27.8 | 3300.3 | 2390.7 | 1974.3 | 1041 | 36.1 |
| | *C* | 2726 | 0 | 442 | 2042 | 2917 | 2820 |
| | *E* | 98 | 43 | 45 | 92 | 266 | 112 |
| J7F07 | *Z* | 26.1 | 2294.8 | 1986.4 | 1645 | 543 | 22.1 |
| | *C* | 5000 | 376 | 265 | 2426 | 5554 | 6188 |
| | *E* | 92 | 36 | 35 | 90 | 98 | 95 |
| J7F08 | *Z* | 30 | 3274.8 | 2561.6 | 2016.6 | 837.8 | 34.1 |
| | *C* | 4379 | 416 | 356 | 1327 | 5205 | 4117 |
| | *E* | 175 | 51 | 48 | 87 | 235 | 156 |
| J7F09 | *Z* | 32.5 | 3262.2 | 2320 | 1682.8 | 886.4 | 26.6 |
| | *C* | 4476 | 27 | — | 3364 | 5246 | 4976 |
| | *E* | 245 | 50 | — | 93 | 119 | 218 |
| J7F10 | *Z* | 28.4 | 3219.5 | 2507.7 | 1530.1 | 710.9 | 34.9 |
| | *C* | 3663 | 74 | 1484 | 2833 | 3007 | 3612 |
| | *E* | 260 | 41 | 48 | 88 | 108 | 224 |
| J7F11 | *Z* | 25.4 | 3252.3 | 1918.5 | 1445.7 | 717.8 | 28.6 |
| | *C* | 3753 | 0 | 54 | 1165 | 1866 | 1816 |
| | *E* | 85 | 38 | 32 | 79 | 99 | 80 |
| J7F12 | *Z* | 30.8 | 3223.4 | 2305.9 | 1515.6 | 915.2 | 52.8 |
| | *C* | 1492 | 8 | 0 | 1329 | 1630 | 1778 |
| | *E* | 117 | 45 | 121 | 110 | 179 | 165 |
| May 2007 | | | | | | | |
| M7F01 | *Z* | 2730.9 | 1891.7 | 1308.3 | 814.6 | 190.5 | 31.9 |
| | *C* | 956 | 545 | 1309 | 2895 | 4171 | 4339 |
| | *E* | 38 | 40 | 48 | 66 | 68 | 70 |
| M7F02 | *Z* | 3331.2 | 2436.3 | 1937.4 | 1262.3 | 520.1 | 34.9 |
| | *C* | 1261 | 540 | 580 | 1601 | 5143 | 6461 |
| | *E* | 78 | 37 | 55 | 75 | 66 | 70 |
| M7F03 | *Z* | 3375.9 | 1909.6 | 1483.9 | 1001 | 385 | 32.3 |
| | *C* | 106 | 393 | 902 | 1971 | 5281 | 6172 |
| | *E* | 46 | 23 | 60 | 137 | 66 | 84 |
| M7F04 | *Z* | 3288.2 | 1935.2 | 1385.8 | 1123.2 | 561.3 | 40.4 |
| | *C* | 179 | 387 | 3292 | 5389 | 7903 | 7707 |
| | *E* | 49 | 146 | 48 | 50 | 95 | 112 |
| M7F05 | *Z* | 3156.2 | 2061.4 | 1424 | 966 | 355.4 | 39.3 |
| | *C* | 217 | 464 | 162 | — | 1498 | 1789 |
| | *E* | 25 | 36 | 32 | — | 57 | 60 |
| M7F06 | *Z* | 3162.3 | 1524.1 | 1121.9 | 871.6 | 379.4 | 25.6 |
| | *C* | 185 | 728 | 1420 | 1454 | 1845 | 1858 |
| | *E* | 69 | 45 | 66 | 69 | 42 | 58 |
| M7F07 | *Z* | 3263.8 | 1514.7 | 1126.5 | 720.3 | 315 | 64.3 |
| | *C* | 193 | 168 | 1540 | 1054 | 1096 | 1019 |
| | *E* | 65 | 31 | 79 | 30 | 100 | 126 |
| M7F08 | *Z* | 3212.4 | 1449.9 | 1024.1 | 676 | 246 | 31.1 |
| | *C* | 125 | 0 | 1208 | 1181 | 1032 | 2195 |
| | *E* | 52 | 208 | 33 | 26 | 78 | 29 |
| M7F09 | *Z* | 3221.2 | 1625.1 | 1391.5 | 1154.8 | 494.5 | 63.6 |
| | *C* | 152 | 3282 | — | 2794 | 3454 | 3256 |
| | *E* | 24 | 81 | — | 62 | 66 | 67 |
| M7F10 | *Z* | 3147.8 | 1990.1 | 1584.2 | 1289.1 | 409.2 | 47.3 |
| | *C* | 0 | 2519 | 1908 | 2074 | 3167 | 4460 |
| | *E* | 100 | 64 | 72 | 78 | 59 | 81 |
| M7F11 | *Z* | 3171.4 | 1258.9 | 953.6 | 687.1 | 386.5 | 31 |
| | *C* | 197 | 1717 | 0 | 1054 | 1088 | 1212 |

TABLE B2. (*Continued*)

| May 2007 | | | | | | | |
|---|---|---|---|---|---|---|---|
| | *E* | 52 | 45 | 23 | 100 | 53 | 59 |
| M7F12 | *Z* | 3101.5 | 1203.2 | 1074.2 | 915.1 | 385.7 | 23.8 |
| | *C* | 178 | 287 | 780 | 1071 | 1205 | 1848 |
| | *E* | 76 | 122 | 34 | 51 | 22 | 98 |
| M7F13 | *Z* | 3158.5 | 1086.9 | 693 | 580.3 | 247.7 | 24.7 |
| | *C* | 957 | 329 | 1125 | 1109 | 1579 | 1565 |
| | *E* | 76 | 63 | 40 | 48 | 56 | 58 |
| M7F14 | *Z* | 3248 | 1311.3 | 1020.3 | 726.5 | 393.8 | 6.2 |
| | *C* | 1162 | 552 | 464 | 608 | 1132 | 1494 |
| | *E* | 136 | 71 | 56 | 75 | 47 | 66 |

| May 2008 | | | | | | |
|---|---|---|---|---|---|---|
| M8F02 | *Z* | 3264 | 1943.8 | 1311.3 | 1128.5 | 994.8 |
| | *C* | 159 | — | 111 | 65 | 222 |
| | *E* | 40 | — | 43 | 51 | 56 |
| | *Z* | 845.2 | 687.2 | 532.2 | 309.4 | 28.4 |
| | *C* | 3208 | 2736 | 3813 | 3038 | 3462 |
| | *E* | 97 | 97 | 150 | 203 | 201 |
| M8F03 | *Z* | 3278 | 1922.6 | 1307.2 | 1141.8 | 992.2 |
| | *C* | 67 | 42 | 197 | 1505 | 2389 |
| | *E* | 23 | 21 | 45 | 69 | 82 |
| | *Z* | 826.3 | 679.9 | 518 | 308.2 | 29.7 |
| | *C* | 3429 | 4376 | 4639 | 5086 | 5234 |
| | *E* | 124 | 170 | 215 | 201 | 310 |
| M8F04 | *Z* | 2940.1 | 1568.6 | 1013.7 | 840.3 | 704.6 |
| | *C* | 73 | 45 | 33 | 2214 | 8554 |
| | *E* | 3 | 8 | 31 | 62 | 86 |
| | *Z* | 533.4 | 377.9 | 220.6 | 129.6 | 28.8 |
| | *C* | 11 673 | 11 524 | 11 084 | 12 028 | 11 936 |
| | *E* | 115 | 141 | 179 | 208 | 211 |
| M8F05 | *Z* | 2950.4 | 1859.1 | 1682.1 | 1447.1 | 1301 |
| | *C* | 105 | 29 | 43 | 547 | 4557 |
| | *E* | 11 | 13 | 32 | 46 | 112 |
| | *Z* | 1130.5 | 839.6 | 523.3 | 215.2 | 28.5 |
| | *C* | 6761 | 9653 | 9028 | 8574 | 8493 |
| | *E* | 104 | 120 | 155 | 160 | 204 |
| M8F06 | *Z* | 24.1* | 19* | 14.8* | 1901.8 | 1297.8 |
| | *C* | 4974 | 4451 | 4071 | 923 | 2613 |
| | *E* | 66 | 74 | 103 | 27 | 53 |
| | *Z* | 1201.1 | 924.1 | 576.3 | 293.1 | 24 |
| | *C* | 2212 | 3114 | 2637 | 3128 | 6369 |
| | *E* | 74 | 90 | 120 | 157 | 187 |
| M8F07 | *Z* | 2928.6 | 1921.6 | 1312 | 833.2 | 720.4 |
| | *C* | 146 | 52 | 50 | 4066 | 3686 |
| | *E* | 17 | 19 | 50 | 64 | 78 |
| | *Z* | 574.1 | 458.8 | 314.2 | 166.5 | 21.4 |
| | *C* | 3416 | — | 5610 | 10 861 | 5522 |
| | *E* | 97 | — | 134 | 219 | 261 |
| M8F08 | *Z* | 2958.3 | 2195.6 | 1927 | 1678.4 | 1552.8 |
| | *C* | 208 | 116 | 5 | 76 | 62 |
| | *E* | 16 | 16 | 40 | 49 | 43 |
| | *Z* | 1337.4 | 1149.4 | 744.5 | 268.7 | 23.3 |
| | *C* | 1512 | 2580 | 4182 | 4433 | 3783 |
| | *E* | 85 | 108 | 167 | 176 | 180 |
| M8F09 | *Z* | 3207.7 | 2290.8 | 1979 | 1752.4 | 1607.6 |
| | *C* | 126 | 190 | 1487 | 2561 | 2747 |
| | *E* | 11 | 24 | 50 | 58 | 84 |
| | *Z* | 1302.4 | 1169.6 | 746.5 | 350.9 | 25.2 |
| | *C* | 3376 | 4238 | 4654 | 5074 | 5597 |

TABLE B2. (*Continued*)

| May 2008 | | | | | | |
|---|---|---|---|---|---|---|
| | *E* | 97 | 185 | 104 | 179 | 183 |
| M8F10 | *Z* | 3198.3 | 2058.6 | 1764.6 | 1644 | 1477.5 |
| | *C* | 239 | 91 | — | 2896 | 4178 |
| | *E* | 40 | 14 | — | 74 | 110 |
| | *Z* | 1217.7 | 856.4 | 541.1 | 241.5 | 26.3 |
| | *C* | 2674 | 2116 | 5347 | 6468 | 6399 |
| | *E* | 83 | 94 | 146 | 224 | 259 |
| M8F11 | *Z* | 3182.8 | 2733.9 | 2458.9 | 2208.1 | 1828.9 |
| | *C* | 61 | 62 | 727 | 1752 | 2555 |
| | *E* | 17 | 24 | 65 | 69 | 92 |
| | *Z* | 1562.8 | 1309.3 | 836.8 | 285.3 | 19.7 |
| | *C* | 2340 | 3243 | 4336 | 4154 | 3993 |
| | *E* | 110 | 139 | 206 | 244 | 418 |
| M8F12 | *Z* | 2940.8 | 2354.4 | 1992.7 | 1931 | 1627.9 |
| | *C* | 156 | 654 | 2041 | 2093 | 2264 |
| | *E* | 11 | 22 | 61 | 67 | 72 |
| | *Z* | 1313.9 | 1010.8 | 683.6 | 38.9 | 35.8 |
| | *C* | 1951 | 3364 | 4335 | 5603 | 4804 |
| | *E* | 401 | 119 | 186 | 281 | 255 |

legacy of the upper part of the previous day's late afternoon profile, which often exhibits a slope in both clear and cloudy conditions. The two case studies demonstrate that radon profiles can vary markedly over the course of a single day, reflecting many important aspects of the evolving boundary layer.

The main conclusion from this study is that vertical radon measurements provide valuable quantitative information regarding mixing and exchange processes in the atmospheric boundary layer under a range of conditions. Indeed, with sufficient vertical resolution, radon measurements are capable of diagnosing features of boundary layer structure that cannot be unambiguously identified using more conventional variables (e.g., the use of wind speed categories to predict poor mixing in the surface layer, or the use of temperature profiles to identify growing morning mixed layers). Conversely, there is a need to consider the structure of the ABL, its connected cloud layers, and its stage of development within the diurnal cycle, when postulating likely vertical distributions of radon for the purposes of regional emission integrations and other studies that rely on estimates of total column radon computed using surface-based radon measurements and supporting meteorological information.

It is hoped that results from this study will be used to quantify ABL mixing processes, improve estimates of vertically integrated radon in surface-based studies, aid in the evaluation of large-eddy simulations and chemical transport models, and ultimately lead to the development of improved parameterizations of vertical transport processes in regional and global climate models.

*Acknowledgments.* The authors acknowledge the important role played by Alan Boyd in the development of the airborne radon sampler and the assistance of Peter Schelander and Ot Sisoutham during the Goulburn field campaigns.

## APPENDIX A

### Laboratory Extraction of Aircraft Radon Samples

The exposed tubes are transported to the flight support laboratory at Lucas Heights, a 2-h drive from Goulburn airport, where the sampled radon is extracted and its activity determined. The principle of the extraction process is similar to Blanchard (1964); key elements of an extraction module are shown in Fig. A1. The sampled radon is heated to 350°C in an electric oven (B) and then transferred from the sampling tube into a smaller ($\sim$100 cm$^3$) charcoal collection trap (F) immersed in a dry ice/ethanol slurry at $-78$°C using conditioned nitrogen (A) as a carrier gas. The nitrogen is conditioned by passing it through a charcoal trap cooled to 0°C to remove any small amounts of radon present. The radon collection trap is then isolated and heated to 450°C, and the released radon is transferred by peristaltic pump (D) to a Lucas scintillation cell (G) in a few consecutive steps by pressure-controlled injections of small amounts of nitrogen. The gas stream is redirected to a second cell to complete the transfer when the pressure in the first cell reaches that of ambient air. Typically, 90% of radon is collected in the first cell, with the transfer process being completed in less than 1 min. Radon in the two cells is allowed to equilibrate with its progeny for 3 h, and activity is then determined by gross alpha scintillation counting for 9 h. To improve throughput, an optimized dual rig is used consisting of two extraction modules running in parallel with collection/transfer cycles 20 min apart. The system throughput is 60 min per sample, allowing processing of two 10-point radon profiles per day for several consecutive days during field campaigns. A calibrated radon source traceable to a NIST standard is used to quantify the efficiency of the two rig modules and the 28 counting channels.

## APPENDIX B

### Vertical Radon Profiles

Table B1 presents metadata characterizing the flights conducted for this study. Table B2 catalogues the aircraft radon profiles. Other auxiliary datasets are available from the authors (surface and aircraft meteorological measurements and Australian land surface radon flux maps).

## REFERENCES

Anderson, R. V., and R. E. Larson, 1974: Atmospheric electric and radon profiles over a closed basin and the open ocean. *J. Geophys. Res.,* **79,** 3432–3435.

Andreae, M. O., H. Berresheim, T. W. Andreae, M. A. Kritz, T. S. Bates, and J. T. Merrill, 1988: Vertical distribution of dimethylsulphide, sulfur dioxide, aerosol ions, and radon over the northwest Pacific Ocean. *J. Atmos. Chem.,* **6,** 149–173.

Balkanski, Y. J., D. J. Jacob, R. Arimoto, and M. A. Kritz, 1992: Distribution of $^{222}$Rn over the North Pacific: Implications for continental influences. *J. Atmos. Chem.,* **14,** 353–374.

Biraud, S., and Coauthors, 2000: European greenhouse gas emissions from continuous atmospheric measurements and radon 222 at Mace Head, Ireland. *J. Geophys. Res.,* **105,** 1351–1366.

Birot, A., J. Fontan, B. Adroguer, D. Blanc, and A. Bouville, 1968: Measurement of radon concentration in the troposphere up to 5000 meters. *Extended Abstracts, Journées d'Electronique de Toulouse,* Toulouse, France, 1–7.

Blanchard, R. L., 1964: An emanation system for determining small quantities of radium-226. U.S. Dept. of Health, Education, and Welfare, Public Health Service Publ. 999-RH-9, 19 pp.

Bradley, W., and J. E. Pearson, 1970: Aircraft measurements of the vertical distribution of radon in the lower atmosphere. *J. Geophys. Res.,* **75,** 5890–5894.

Butterweck, G., A. Reineking, J. Kesten, and J. Porstendörfer, 1994: The use of the natural radioactive noble gases radon and thoron as tracers for the study of turbulent exchange in the atmospheric boundary layer—Case study in and above a wheat field. *Atmos. Environ.,* **28,** 1963–1969.

Chevillard, A., and Coauthors, 2002: Transport of $^{222}$Rn using the regional model REMO: A detailed comparison with measurements over Europe. *Tellus,* **54B,** 850–871.

Cohen, L. D., S. Barr, R. Krablin, and H. Newstein, 1972: Steady-state vertical turbulent diffusion of radon. *J. Geophys. Res.,* **77,** 2654–2668.

Considine, D. B., D. J. Bergmann, and H. Liu, 2005: Sensitivity of Global Modeling Initiative chemistry and transport model simulations of radon-222 and lead-210 to input meteorological data. *Atmos. Chem. Phys.,* **5,** 3389–3406.

Crawford, J., W. Zahorowski, and D. D. Cohen, 2008: A new metric space incorporating radon-222 for generation of back trajectory clusters in atmospheric pollution studies. *Atmos. Environ.,* **43,** 371–381.

Dentener, F., J. Feichter, and A. Jeuken, 1999: Simulation of the transport of Rn-222 using on-line and off-line global models at different horizontal resolutions: A detailed comparison with measurements. *Tellus,* **51B,** 573–602.

Draxler, R. R., and G. D. Hess, 1998: An overview of the HYSPLIT-4 modelling system for trajectories, dispersion and deposition. *Aust. Meteor. Mag.,* **47,** 295–308.

Filippi, D., 2000: Etude et développement d'un instrument aéroporté destiné à la collecte des aérosols et à la mesure du $^{222}$Rn par son dépôt actif. Ph.D. dissertation, Université Paris 6 Pierre et Marie Curie, 267 pp.

Forster, C., A. Stohl, and P. Seibert, 2007: Parameterization of convective transport in a Lagrangian particle dispersion model and its evaluation. *J. Appl. Meteor. Climatol.,* **46,** 403–422.

Garratt, J. R., 1992: *The Atmospheric Boundary Layer.* Cambridge University Press, 316 pp.

Gaudry, A., G. Polian, B. Ardouin, and G. Lambert, 1990: Radon-calibrated emissions of $CO_2$ from South Africa. *Tellus,* **42,** 9–19.

Gogolak, C. V., and H. L. Beck, 1980: Diurnal variations of radon daughter concentrations in the lower atmosphere. Natural radiation environment III, U.S. Department of Energy Rep. CONF-780422, 259–280.

Griffiths, A. D., W. Zahorowski, A. Element, and S. Werczynski, 2010: A map of radon flux at the Australian land surface. *Atmos. Chem. Phys.,* **10,** 8969–8982.

Guedalia, D., C. Allet, and J. Fontan, 1974: Vertical exchange measurements in the lower troposphere using ThB (Pb-212) and radon (Rn-222). *J. Appl. Meteor.,* **13,** 27–39.

Gupta, M. L., A. R. Douglass, S. Randolph Kawa, and S. Pawson, 2004: Use of radon for evaluation of atmospheric transport models: Sensitivity to emissions. *Tellus,* **56B,** 404–412.

Hosler, C. R., 1968: Urban–rural climatology of atmospheric radon concentrations. *J. Geophys. Res.,* **73,** 1155–1166.

Israël, H., 1951: Radioactivity of the atmosphere. *Compendium of Meteorology,* T. F. Malone, Ed., Amer. Meteor. Soc., 155–161.

Jacob, D. J., and M. J. Prather, 1990: Radon-222 as a test of convective transport in a general circulation model. *Tellus,* **42B,** 118–134.

——, and Coauthors, 1997: Evaluation and intercomparison of global atmospheric transport models using $^{222}$Rn and other short-lived tracers. *J. Geophys. Res.,* **102,** 5953–5970.

Jacobi, W., and K. André, 1963: The vertical distribution of radon-222, radon-220, and their decay products in the atmosphere. *J. Geophys. Res.,* **68,** 3799–3814.

Jonassen, N., and M. H. Wilkening, 1970: Airborne measurements of radon 222 daughter ions in the atmosphere. *J. Geophys. Res.,* **75,** 1745–1752.

Kirichenko, L. V., 1962: The vertical distribution of the products of decay of radon in the free atmosphere. Problems of nuclear meteorology, I. L. Karol and S. G. Malakhov, Eds., United States Atomic Energy Commission, Division of Technical Information Rep. AEC-TR-6128, 92–124.

——, 1970: Radon exhalation from vast areas according to vertical distributions of its short-lived decay products. *J. Geophys. Res.,* **75,** 3639–3649.

Koch, D., G. A. Schmidt, and C. V. Field, 2006: Sulfur, sea salt, and radionuclide aerosols in GISS ModelE. *J. Geophys. Res.,* **111,** D06206, doi:10.1029/2004jd005550.

Kritz, M. A., J.-C. Le Roulley, and E. F. Danielsen, 1990: The China Clipper—Fast advective transport of radon-rich air from the Asian boundary layer to the upper troposphere near California. *Tellus,* **42B,** 46–61.

——, S. W. Rosner, K. K. Kelly, M. Loewenstein, and K. R. Chan, 1993: Radon measurements in the lower tropical stratosphere: Evidence for rapid vertical transport and dehydration of tropospheric air. *J. Geophys. Res.,* **98,** 8725–8736.

——, ——, and D. Z. Stockwell, 1998: Validation of an off-line three-dimensional chemical transport model using observed radon profiles: 1. Observations. *J. Geophys. Res.,* **103,** 8425–8432.

Lambert, G., G. Polian, J. Sanak, B. Ardouin, A. Buisson, A. Jegou, and J.-C. Le Roulley, 1982: Cycle du radon et de ses descentants: Application à l'étude des échanges troposphère-stratosphère. *Ann. Geophys.,* **38,** 497–531.

——, J.-C. Le Roulley, and M. A. Kritz, 1990: Box model for radon transfers into the stratosphere. *Tellus,* **42B,** 135–141.

Larson, R. E., 1974: Radon profiles over Kilauea, the Hawaiian Islands, and Yukon Valley snow cover. *Pure Appl. Geophys.,* **112,** 204–208.

——, and W. A. Hoppel, 1973: Radon-222 measurements below 4 km as related to atmospheric convection. *Pure Appl. Geophys.,* **105,** 900–906.

Lee, H. N., and R. J. Larson, 1997: Vertical diffusion in the lower atmosphere using aircraft measurements of $^{222}$Rn. *J. Appl. Meteor.,* **36,** 1262–1270.

LeMone, M. A., and W. T. Pennell, 1976: The relationship of trade wind cumulus distribution to subcloud layer fluxes and structure. *Mon. Wea. Rev.,* **104,** 524–539.

Li, Y., and J. S. Chang, 1996: A three-dimensional global episodic tracer transport model: 1. Evaluation of its transport processes by radon 222 simulations. *J. Geophys. Res.,* **101,** 25 931–25 947.

Lin, X., F. Zaucker, E.-Y. Hsie, M. Trainer, and S. A. McKeen, 1996: Radon-222 simulations as a test of a three-dimensional regional transport model. *J. Geophys. Res.,* **101,** 29 165–29 177.

Liu, S. C., J. R. McAfee, and R. J. Cicerone, 1984: Radon-222 and tropospheric vertical transport. *J. Geophys. Res.,* **89,** 7291–7297.

Machta, L., 1963: Radon and other radioisotopes in the atmosphere. *J. Geophys. Res.,* **68,** 3815.

——, and H. F. J. Lucas, 1962: Radon in the upper atmosphere. *Science,* **135,** 296–299.

Mahrt, L., 1976: Mixed layer moisture structure. *Mon. Wea. Rev.,* **104,** 1403–1407.

Miranda, H. A. J., 1957: The radon content of the atmosphere in the New York area as measured with an improved technique. *J. Atmos. Terr. Phys.,* **11,** 272–283.

Moeng, C.-H., and J. C. Wyngaard, 1984: Statistics of conservative scalars in the convective boundary layer. *J. Atmos. Sci.,* **41,** 3161–3169.

Moore, H. E., S. E. Poet, and E. A. Martell, 1973: $^{222}$Rn, $^{210}$Pb, $^{210}$Bi, and $^{210}$Po profiles and aerosol residence times versus altitude. *J. Geophys. Res.,* **78,** 7065–7075.

——, ——, and ——, 1977: Vertical profiles on $^{222}$Rn and its long-lived daughters over the eastern Pacific. *Environ. Sci. Technol.,* **11,** 1207–1210.

Moses, H., A. F. Stehney, and H. F. J. Lucas, 1960: The effect of meteorological variables upon the vertical and temporal distributions of atmospheric radon. *J. Geophys. Res.,* **65,** 1223–1238.

Nazarov, L. E., A. F. Kuzenkov, S. G. Malakhov, L. A. Volokitina, Y. I. Gaziyev, and A. S. Vasil'yev, 1970: Radioactive aerosol distribution in the middle and upper troposphere over the USSR in 1963–1968. *J. Geophys. Res.,* **75,** 3575–3588.

Negro, V. C., N. Y. Chiu, R. J. Larsen, S. B. Wurms, and C. Breheny, 1996: Continued testing and evaluation of the Radgrabber. USDOE Rep. EML-580, 153 pp.

Nguyen, B. C., G. Lambert, G. Polian, and J. P. Jacquin, 1967: Radon-222 vertical profiles comparison from 0 to 4400 m over Atlantic Ocean (in French). *C. R. Acad.,* **265B,** 428–433.

Nicholls, S., and M. A. LeMone, 1980: The fair weather boundary layer in GATE: The relationship of subcloud fluxes and structure to the distribution and enhancement of cumulus clouds. *J. Atmos. Sci.,* **37,** 2051–2067.

Ötles, Z., and J. A. Young, 1996: Influence of shallow cumuli on subcloud turbulence fluxes analyzed from aircraft data. *J. Atmos. Sci.,* **53,** 665–676.

Pereira, E. B., D. J. R. Nordemann, S. C. Wofsy, and S. Trumbore, 1988: Vertical radon concentration profiles over the Brazilian Amazon Basin during the wet season. *Eos, Trans. Amer. Geophys. Union,* **69** (Spring Meeting Suppl.), Abstract A52-03.

Perry, K. D., T. A. Cahill, R. C. Schnell, and J. M. Harris, 1999: Long-range transport of anthropogenic aerosols to the National Oceanic and Atmospheric Administration baseline station at Mauna Loa Observatory, Hawaii. *J. Geophys. Res.,* **104,** 18 521–18 533.

Polian, G., G. Lambert, B. Ardouin, and A. Jegou, 1986: Long-range transport of continental radon in subantarctic and arctic areas. *Tellus,* **38,** 178–189.

Puri, K., G. S. Dietachmayer, G. A. Mills, N. E. Davidson, R. A. Bowen, and L. W. Logan, 1998: The new BMRC limited area prediction system, LAPS. *Aust. Meteor. Mag.,* **47,** 203–223.

Ramonet, M., J.-C. Le Roulley, P. Bousquet, and P. Monfray, 1996: Radon-222 measurements during the Tropoz II campaign and comparison with a global atmospheric transport model. *J. Atmos. Chem.,* **23,** 107–136.

Rasch, P. J., and Coauthors, 2000: A comparison of scavenging and deposition processes in global models: Results from the WCRP Cambridge Workshop of 1995. *Tellus,* **52B,** 1025–1056.

Schery, S. D., and S. Huang, 2004: An estimate of the global distribution of radon emissions from the ocean. *Geophys. Res. Lett.,* **31,** L19104, doi:10.1029/2004GL021051.

Schmidt, M., R. Graul, H. Sartorius, and I. Levin, 1996: Carbon dioxide and methane in continental Europe: A climatology and $^{222}$Radon-based emission estimates. *Tellus,* **48,** 457–473.

Stull, R. B., 1985: A fair-weather cumulus cloud classification scheme for mixed-layer studies. *J. Climate Appl. Meteor.,* **24,** 49–56.

——, 1988: *An Introduction to Boundary Layer Meteorology*. Kluwer Academic, 666 pp.

Turekian, K. K., Y. Nozaki, and L. K. Benninger, 1977: Geochemistry of atmospheric radon and radon products. *Annu. Rev. Earth Planet. Sci.,* **5,** 227–255.

Wexler, H., L. Machta, D. H. Pock, and F. D. White, 1956: Atomic energy and meteorology. *Proc. First Int. Conf. on the Peaceful Uses of Atomic Energy,* Geneva, Switzerland, International Atomic Energy Agency, 333–344.

Wigand, A., and F. Wenk, 1928: Der Gehalt der Luft an Radium-Emanation, nach Messungen bei Flugzeugaufstiegen. *Ann. Lpz. Phys.,* **86,** 657–686.

Wilkening, M. H., 1956: Variation of natural radioactivity in the atmosphere with altitude. *Trans. Amer. Geophys. Union,* **37,** 177–180.

——, 1970: Radon 222 concentrations in the convective patterns of a mountain environment. *J. Geophys. Res.,* **75,** 1733–1740.

——, and G. W. Paltridge, 1967: Radon sampling technique for the study of orographic cumuli. *Trans. Amer. Geophys. Union,* **48,** 105.

Williams, A. G., S. D. Chambers, W. Zahorowski, J. Crawford, K. Matsumoto, and M. Uematsu, 2009: Estimating the Asian radon flux density and its latitudinal gradient in winter using ground-based radon observations at Sado Island. *Tellus,* **61B,** 732–746.

Wyngaard, J. C., and R. A. Brost, 1984: Top-down and bottom-up diffusion of a scalar in the convective boundary layer. *J. Atmos. Sci.,* **41,** 102–112.

Zahorowski, W., and S. Whittlestone, 1996: A fast portable emanometer for field measurements of radon and thoron flux. *Radiat. Prot. Dosimetry,* **67,** 109–120.

——, and ——, 1999: Radon database 1987–1996: A review. *Baseline Atmospheric Program (Australia) 1996,* J. L. Gras et al., Eds., Bureau of Meteorology and CSIRO Atmospheric Research, 71–80.

——, S. D. Chambers, and A. Henderson-Sellers, 2004: Ground based radon-222 observations and their application to atmospheric studies. *J. Environ. Radioact.,* **76,** 3–33.

——, and Coauthors, 2005: Radon-222 in boundary layer and free tropospheric continental outflow events at three ACE-Asia sites. *Tellus,* **57,** 124–140.

——, A. G. Williams, A. T. Vermeulen, S. D. Chambers, J. Crawford, and O. Sisoutham, 2008: Diurnal boundary layer mixing patterns characterised by radon-222 gradient observations at Cabauw. *Extended Abstracts, 18th Conf. on Boundary Layers and Turbulence,* Stockholm, Sweden, Amer. Meteor. Soc., 9B.2. [Available online at http://ams.confex.com/ams/18BLT/techprogram/paper_139978.htm.]

Zaucker, F., P. H. Daum, U. Wetterauer, C. Berkowitz, B. Kromer, and W. S. Broecker, 1996: Atmospheric $^{222}$Rn measurements during the 1993 NARE intensive. *J. Geophys. Res.,* **101,** 29 149–29 164.